Master's Thesis

Calibration of a Heterodyne Dual Frequency Comb Laser Absorption Spectroscopy System

Kalibrierung eines Systems zur Laserabsorptionsspektroskopie basierend auf multi-heterodynen Doppel-Frequenzkämmen

prepared by

Leni Schmidt

from Bassum

at the German Aerospace Center
Institute of Aerodynamics and Flow Technology
Department Spacecraft

Date of Submission: 17.01.2023

Supervisor: Dr. Jan Martinez Schramm

First Referee: Prof. Dr. Dr. Andreas Dillmann

Second Referee: Prof. Dr. Martin Rein

Table of Contents

Abstract

The use of hydrogen combustion based scramjets for propulsion is one promising idea to drive hypersonic passenger transport. Even though these propulsion systems prevent CO_2 formation, the production of NO and H_2O during the combustion process may have other environmental effects. Therefore, the experimental determination of the production and the atmospheric release of NO and H_2O in hydrogen combustion is of interest for the study of scramjet models in the High Enthalpy Shock Tunnel Göttingen. A new laser absorption spectroscopy method uses quantum cascade lasers (QCLs) in the infrared region within μ-second range. The method is based on the creation of heterodyne beating by two frequency combs. But the measurement technique requires a further calibration and understanding of the measurement modes. By modulating current and temperature of the lasers and thus sweeping through them, the spectral point spacing is reduced, resulting in a higher resolution and better foundation for the detection of gas concentrations. This work presents experimental prerequisites and results from tests with a multipass absorption cell in internal and external set-up for testing the influence of optical fibers. The fibers as well as additional optics are essential to bring the light beam from the spectrometer towards an external test section and back to a detector.

Keywords: laser absorption spectroscopy, frequency comb, heterodyne, sweeping, hydrogen combustion, optical fibers

Zusammenfassung

Der Einsatz von Scramjets mit Wasserstoffverbrennung ist eine vielversprechende Idee für zukünftige Antriebe im Hyperschall-Personenverkehr. Während diese Antriebssysteme die Bildung von CO_2 verhindern, kann die Entstehung von NO und H_2O während der Verbrennung sowie deren Freisetzung in der Atmosphäre andere Auswirkungen auf die Umwelt haben. Daher ist die experimentelle Bestimmung der NO- und H_2O-Entstehung bei der Wasserstoffverbrennung für die Untersuchung von Scramjet-Modellen im Hochenthalpiekanal in Göttingen von Interesse. Eine neue Methode ist Laserabsorptionsspektroskopie mittels Quantenkaskadenlasern (QCLs) im Infrarotbereich im µs-Bereich, die auf der Erzeugung von Schwebungssignalen durch zwei Frequenzkämme beruht. Vor der tatsächlichen Anwendung erfordert die Methode eine tiefergehende Kalibrierung und ein Verständnis der Messmodi. Durch die Modulation von Strom und Temperatur der Laser und das damit verbundene „Sweeping" wird der spektrale Punktabstand verringert, was zu einer höheren Auflösung und einer besseren Grundlage für den Nachweis von Gaskonzentrationen führt. In dieser Arbeit werden die experimentellen Voraussetzungen und Ergebnisse von Tests mit einer Multipass-Absorptionszelle in internem und externem Aufbau vorgestellt und insbesondere der Einfluss von Lichtleitern untersucht. Die Lichtleiter sowie zusätzliche optische Elemente sind essenziell, um den Lichtstrahl vom Spektrometer hin zu einem externen Messbereich und zurück auf einen Detektor zu bringen.

Schlüsselworte: Laserabsorptionsspektroskopie, Frequenzkamm, Schwebung, Sweeping, Wasserstoffverbrennung, Lichtleiter

Acknowledgements

Nomenclature

Greek symbols

λ	wavelength	m
υ	wavenumber	cm^{-1}
ρ	density	kg/m^3
τ	round-trip time	s
φ	phase	rad
ω	angular frequency	rad/s

Latin symbols

A	envelope function	-
A'	absorbance	-
E	energy	J
f	frequency	Hz
I	intensity	-
L	cavity length	m
l	path length	m
p	pressure	bar
t	time	s
T	temperature	K, °C
V	volume	m^3
v	velocity	m/s

Abbreviations

CFD	computational fluid dynamics
DLR	German Aerospace Center
FTIR	Fourier transform infrared (spectroscopy)
FWM	four-wave mixing
HAPI	HITRAN Application Programming Interface
HEG	High Enthalpy Shock Tunnel, Göttingen
HITRAN	*Hi*gh-resolution *tran*smission molecular absorption database
LAS	laser absorption spectroscopy
ONERA	Office National d'Etudes et de Recherches Aérospatiales, French national aerospace research center
RF	radio frequency
RMS	root mean square
SNR	signal-to-noise ratio
TDLAS	tunable diode laser absorption spectroscopy
QCL	quantum cascade laser

Chemical Elements

Symbol	Element
CO_2	carbon dioxide
H_2	hydrogen
H_2O	water
He	helium
N_2	nitrogen
NO_x	nitrogen oxides
NO	nitric oxide
N_2O	nitrous oxide
O_2	oxygen
O_3	ozone
OH	hydroxyl

1. Introduction

In history, hydrogen-fueled aircraft were first found to be used in aeronautics for the inflation of balloons instead of using hot air as lifting medium. Since the late 1930s, research in the field of hydrogen powered aircraft was initiated by the tests of the first turbojet engine fueled with hydrogen. Every once in a while, hydrogen as a fuel renewed its interested, yielding the start of several projects that covered possible design and system analysis for engines operating on hydrogen. [1]

Nowadays, the concerns about the man-made global warming and the long-term lack of fossil fuels arise the need for "green fuels" using emission-free fuels instead of systems based on kerosene combustion. Combined with the economic desire to reduce flight times, new flight concepts for hydrogen-fueled supersonic airbreathing vehicles are developed and tested around the world. Hydrogen was identified to be an attractive option to decarbonize the civil aviation as it is widely available and does not produce carbon dioxide (CO_2) during the flight. The hydrogen-fueled engines only emit water vapor and nitrogen oxides (NO_x), in particular nitric oxide (NO). As the aim is to create a low or even neutral climate impact, a relevant part of the research is the evaluation of environmental effects. For that, it is crucial to determine the produced concentrations of gas species during the hydrogen burning. There are various numerical models and simulations for that, implementing the chemical reaction mechanisms occurring at hydrogen combustion. But the complexity of gas kinetics requires a reliable experimental validation for the numerical results. An experimental technique for experiments at test facilities needs to fulfill high requirements regarding accuracy and quality.

A typical strategy to determine gas species concentrations is the application of the measurement technique of laser absorption spectroscopy. As absorption is characteristic for each gas species, the comparison of a reference beam with a beam transmitted through a sample allows the identification of a gas species and its concentration for known surrounding thermal properties. Absorption lines of fundamental interest are located in the infrared regime. Since these optical light frequencies oscillate 10^5 times faster than conventional detectors can resolve, it is a challenge to perform accurate frequency measurements in that optical range [2]. A new approach is laser absorption spectroscopy using heterodyne signals

created by the combined use of two frequency combs. The heterodynes lie in the radio frequency domain and thus are detectable. By this link between optical and radio frequency domain, a reconstruction of the absorption features in the optical domain is possible.

In 2020, the general applicability of the new technique was shown for experiments conducted in the High Enthalpy Shock Tunnel (HEG) at the DLR site in Göttingen [3]. The HEG is one of the major European hypersonic wind tunnels and is able to reproduce correct absolute flow speeds up to 7 km/s and hence recreates the realistic gas temperatures. As typical test times in HEG are in the order of milliseconds, the experimental methods need to have a high temporal resolution. Dual comb laser absorption spectroscopy allows for that. The tests carried out showed that the technique is suitable for measurements during the experiment but a deepened understanding and calibration of the spectrometer and its different measurement modes for higher spectral resolution is favorable.

Chapter 2 of this Master's thesis reports the theoretical background for the spectroscopic technique itself and the related physics, including basics of the operation principle of a QCL and frequency combs. Furthermore, it gives a general introduction to the topic of absorption of NO and H_2O during combustion.

The spectrometer device and the experimental setup used for conducting the measurements are presented in chapter 3. In the scope of this work, calibration measurements are performed in a laboratory set-up using a multipass absorption cell. A major focus lies in the identification of error sources and necessities for the successful performance of both calibration and actual HEG measurements. The work covers test cases for two different measurement modes. While the *LongTerm* mode is the basic mode for static measurements, the *StepSweeping* mode aims to increase the spectral resolution by modulation of current. The tests are carried out in an internal and external set-up to study the influence of additional fiber optics which are necessary to guide the laser beam in and out the spectrometer towards an external test section. It is important to study whether and how both the signal and the measurement quality are influenced by the use of fibers.

The obtained experimental results are described and analyzed in detail in chapter 4. Finally, a conclusion as well as an outlook by formulating future work aspects are given in chapter 5.

2. Dual Comb Laser Absorption Spectroscopy

Laser absorption spectroscopy is a measurement technique that uses lasers to assess the amount of a species in a gas sample by its absorption features. Modern spectrometers that are suitable for the infrared regime employ so-called frequency combs to measure with high accuracy and high acquisition rates in the µs range. As the generation of such combs requires mode-locked lasers, the development of stable quantum cascade lasers contributed to a major advance in mid-infrared laser absorption spectroscopy regarding temporal and spectral accuracy.

2.1.   LAS Measurement Technique and Related Physics

Electromagnetic radiation is energy that propagates as electrical and magnetic waves. The radiation includes visible light as well as infrared (IR), UV and microwave radiation. A typically applied parameter to characterize the electromagnetic radiation is the wavelength λ. The unit µm is the most used for measurements in the mid-infrared region. The wavelength is related to the wavenumber $\tilde{\nu}$ that indicates the number of waves per unit length. This parameter expressed in cm^{-1} is the number of waves in a 1 cm-long wavetrain [4]:

$$\tilde{\nu} = \frac{1}{\lambda[\text{cm}]} = \frac{1 \cdot 10^4}{\lambda[\text{µm}]} \ . \tag{2.1}$$

As another parameter for the wave motion, the frequency ν describes the number of oscillations of the radiation vector per unit of time in s^{-1}. The frequency ν and the wavelength λ are correlated by the speed of light c given in units of cm s^{-1}:

$$\nu = \frac{c}{\lambda}. \tag{2.2}$$

As the speed of light is defined to have a precise value, the conversion between frequency and wavelength can be done without loss in accuracy.

Due to the relation of wavenumber $\tilde{\nu}$ and wavelength λ, the wavenumber can be expressed

proportional to the frequency and thus to the energy of the electromagnetic alternating field:

$$\tilde{\nu} = \frac{\nu}{c} \,. \tag{2.3}$$

In IR spectroscopy, wavenumbers are usually given in units of reciprocal centimeters (cm^{-1}). The proportionality constant between the energy E and the radiation frequency is Planck's constant $h = 6.626 \cdot 10^{-34}$ Js:

$$E = h \cdot \nu. \tag{2.4}$$

When matter interacts with an electromagnetic wave, energy can be transferred by absorption of the radiation energy in the molecular system of the material. This energy transfer is dependent on the different atomic and molecular structures.

According to Bohr's atomic model, negatively charged electrons following elliptical orbits encircle a positively charged nucleus in an atom. The energy of these electrons is quantized, meaning that each of the electron orbits has a specific energy content E. An electron's jump between two orbits results in an uptake or release of the energy difference existing between the orbits:

$$\Delta E = E_1 - E_2. \tag{2.5}$$

Here, E_1 and E_2 denote the energy in orbit 1 and 2, respectively. The interaction with radiation is the main mechanism for an uptake of energy. Due to the quantized energy levels of the atom, the radiation's frequency needs exactly to match the energy difference between two orbits. This condition can be written as

$$E_1 - E_2 = h \cdot \nu. \tag{2.6}$$

The release of energy for the transition to a lower energy level happens through the emission of radiation that is characterized by a frequency corresponding to the energy difference according to eq. (2.6). A molecule is a compound consisting of two or more atoms. Besides the electronic transition, an uptake of energy in a molecule can result in vibrational and rotational excitations. Both these transitions are as well quantized and must fulfill the frequency condition given by eq. (2.6).

Usually, the atoms in a molecule are bound together at particular distances which are defined by all the forces acting between the atoms. When the molecule absorbs certain amounts of energy, the atoms can be exited to vibrate around their state of equilibrium. The vibrational frequency depends on the atomic masses and the binding forces between them. The necessary energy contents and thus radiation frequencies belong to the IR radiation region and cover wavenumbers between 12800 cm^{-1} and 200 cm^{-1} [4]. The excitation of molecular rotation requires less energy than the vibrational excitation. The suitable frequencies lie in the far-infrared but mostly in the microwave region.

Spectroscopy now simply utilizes the interaction between gases and electromagnetic radiation to draw a conclusion on the mass concentration of a specific species in a gas sample. The absorption spectrum of a sample is the fraction of incident radiation absorbed by the material over a range of frequencies of electromagnetic radiation. The frequencies where absorption occurs are determined by the atomic and molecular structure of the sample. At these specific frequencies, the radiation's energy is equivalent energy difference needed for a transition between two quantum mechanical states of the sample.

Mathematically, the attenuation of the intensity of radiation when passing through a medium or sample due to the occurring absorption can be described by using the Lambert-Beer law. When a light beam with an intensity I dependent on spectral frequency f passes through a sample with an absorption coefficient α, the intensity is reduced by

$$\frac{\mathrm{d}I}{\mathrm{d}z} = -\alpha \cdot I. \tag{2.7}$$

in an absorbing layer with thickness $\mathrm{d}z$. By assuming that α does not depend on I, the integration of eq. (2.7). within $z = 0$ to $z = l$ leads to the general form of the Lambert-Beer law:

$$I = I_0 \cdot e^{-\alpha \cdot l} \tag{2.8}$$

where I_0 denotes the incident intensity. The Lambert-Beer law is often converted to the logarithm base 10 instead of the natural logarithm.

The logarithm of the dimensionless intensity ratio I/I_0 is used for the definition of the absorbance A':

$$A' = -log_{10}\left(\frac{I}{I_0}\right) = -\epsilon \cdot c \cdot l. \tag{2.9}$$

Here, ϵ denotes the molar absorptivity, c is the species concentration and l is the path length.

Traditional laser absorption spectroscopy operates only at a single wavelength, therefore limits the measurement range but features a high resolution by narrow linewidths. The first disadvantage can be overcome by applying Fourier Transform Infrared spectroscopy (FTIR) which allows measurements over a wide spectral range [4]. Instead of using monochromatic light, a beam composed of many frequencies is employed.

Conceptually, the light generated by an IR broadband source passes through a Michelson interferometer. Inside the interferometer, the beam is divided by a beam splitter. Each of the beams is reflected at a mirror and propagates back towards the beam splitter, where the beams are combined again with superposition principle. While one part is reflected at a fixed mirror, the other part hits a movable mirror. As the mirror moves, the changed path difference results in different interference patterns. The light travels through a sample onto a detector. The obtained amplitude raw data in the time domain, the so-called interferogram, are converted to spectra in the frequency domain by performing a Fourier transformation.

Since the classical Fourier spectrometer includes moving parts, leading to a limited acquisition speed, and has no optimal spectral resolution due to broader linewidths, other types of infrared spectroscopy are subject of investigations. In particular, spectroscopy by means of optical frequency combs surpassed the precision and speed of Fourier spectrometers.

2.2. Frequency Combs for Dual-Comb LAS

In the context of molecular FTIR spectroscopy, the advancement of frequency comb laser sources for dual-comb spectroscopy results in clear improvement of measurement times and allows acquisition rates in the order of μs. As part of frequency metrology, frequency combs were first introduced to improve the precision of frequency measurements [5]. In 2005, the

scientists Hänsch and Hall were awarded the Nobel Prize for their contribution to the advancement of frequency combs [6]. The optical frequency-combs broke new grounds for many subjects including fundamental time metrology, spectroscopy and frequency synthesis [2].
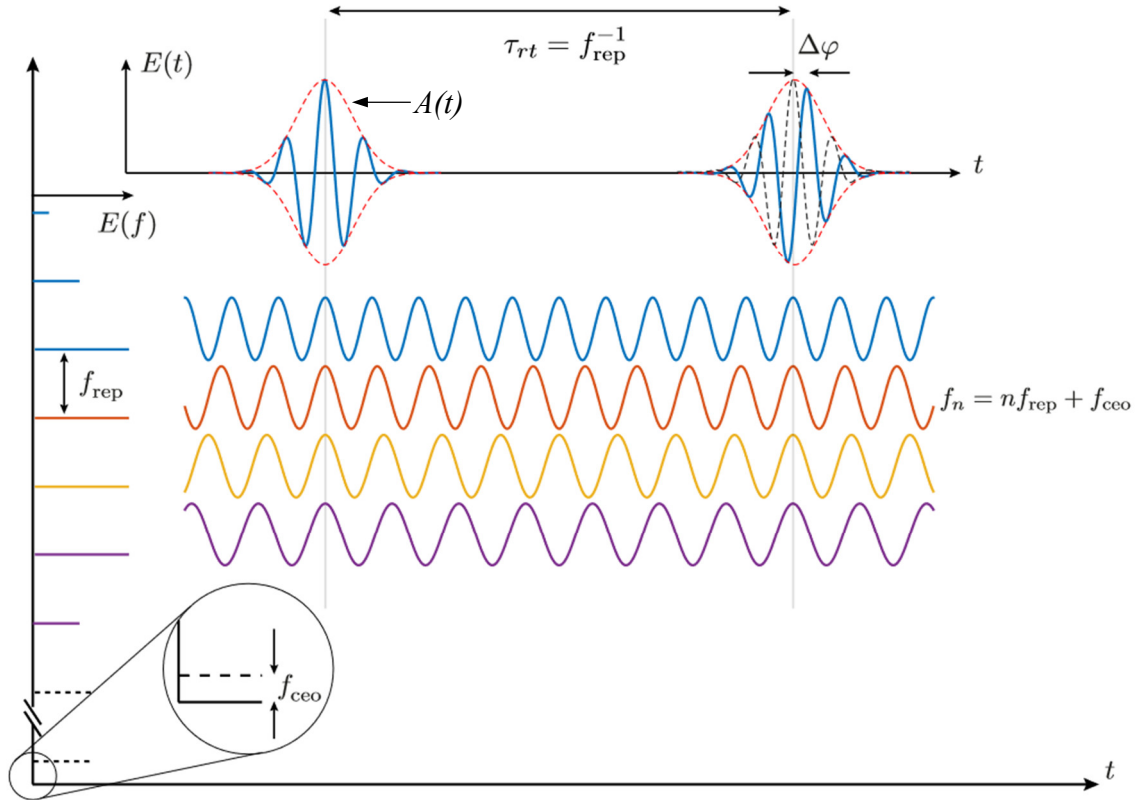
Fig. 1: Principle of a frequency comb. Adapted from [7].

An optical frequency comb consists of periodic coherent radiation with spectra that are characterized by perfectly equidistant modes in the frequency domain. The sharp spectral lines that are spaced by the repetition frequency f_{rep}. Due to their spike-like appearance they are named "comb". Historically, frequency combs are formed by a mode-locked laser, whereas there are today other forms of comb-generation are possible. But considering the ideal case of a femtosecond mode-locked laser provides an intuitive picture of the working principle of a frequency comb [7]. In a mode-locked laser, a narrow pulse propagates in a laser cavity of length L. As illustrated in **Fig. 1** with the red solid line, the pulse is defined by its envelope $A(t)$ (of the electric field $E(t)$) and a carrier envelope angular frequency $\omega_c = 2\pi f_c$. Every time the pulse reaches one of the cavity's mirrors, a fraction of the pulse couples out, thus generating a train of pulses as the output of the laser. The round-trip time

τ_{rt} determines the distance between two pulses, which allows the definition of a comb repetition frequency as:

$$f_{rep} = \frac{1}{\tau_{rt}} = \frac{v_g}{2L}.$$

(2.10)

But the carrier wave of the pulse, which is shown as blue solid line in **Fig. 1**, propagates with a phase velocity v_{ph} inside the cavity. Phase velocity v_{ph} and group velocity v_g differ due to arising dispersion, resulting in a shift of the E-field with respect to the pulse envelope with a phase difference $\Delta\varphi$. Hence, while the E-field itself is not periodic as function of time, the envelope can be assumed periodic. The E-field $E(t)$ outside the cavity is given by:

$$E(t) = A(t)e^{-i\omega_c t} + cc. = \sum_n A_n e^{-i(n\omega_{rep}+\omega_c)t} + cc.$$

(2.11)

Here, A_n denote the Fourier components of the envelope $A(t)$ and $\omega_{rep} = 2\pi f_{rep}$. Eqn. (2.11) shows that the laser spectrum consists of a comb of frequencies separated by the comb repetition frequency f_{rep}. But the comb does not correspond to exact harmonics of the repetition frequency, as ω_c is not an integer multiple of ω_{rep}. Instead, the comb of frequencies is shifted by an offset ω_{ceo}, which originates in a carrier-to-envelope phase slippage [7]. By evaluating the E-field at t and $t + \tau_{rt}$ in eqn. (2.11), the following relation is obtained:

$$f_{ceo} = \frac{\Delta\varphi f_{rep}}{2\pi}.$$

(2.12)

As conclusion, each frequency line f_n of such a frequency comb can be expressed with

$$f_n = f_{ceo} + n \cdot f_{rep}$$

(2.13)

where the frequencies are shifted by the so-called carrier-envelope offset frequency f_{ceo} [8]. Because of the extremely stable repetition rate of the laser f_{rep}, the line-to-line frequency noise of an optical frequency comb is correlated. Compared to an array of single-frequency laser where the frequency noise between individual lines is uncorrelated, a frequency comb allows measurements with a much smaller linewidth [9].

The spectrum E(f) of the E-field E(t) is obtained by applying the Fourier transformation [10]:

$$E(f) = \mathcal{F}\big(E(t)\big) = \sum_n A_n e^{i\Delta\varphi} \delta\big(f - nf_{rep} - f_{ceo}\big).$$

(2.14)

The intensity spectrum is illustrated in **Fig. 1** on the vertical axis, where each mode can be attributed to a corresponding optical frequency.

Dual-comb spectroscopy applies the optical frequency comb in order to provide a high resolution and high sensitivity. **Fig. 2** shows a schematic of the principle of this spectroscopic technique. By using two frequency combs with slightly different repetition rates $f_{rep,1}$ and $f_{rep,2}$, a heterodyne beating signal is created with frequency

$$\Delta f_{rep} = f_{rep,2} - f_{rep,1}. \tag{2.15}$$

Whereas the optical frequencies of the combs cannot be detected directly, the difference frequencies lie in the RF domain, thus they fall within the bandwidth limit of frequency counters [2]. By correctly aligning the combs, a photo-detector can be used to measure the heterodyne beating that contains information about the sample absorption. The dual-comb spectrometer measures at frequencies spaced by the comb repetition rate which defines the resolution of the technique. For example, a comb with repetition rate f_{rep}= 7.5 GHz yields a resolution of 0.25 cm^{-1} [9]. As this often is not sufficient for applications in gas spectroscopy of small molecules, a higher resolution is obtained by sweeping the comb over its repetition frequency f_{rep}. The variation of either the laser current or temperature of one or both combs changes the comb spacing Δf_{rep}, thus resulting in an increased resolution [8].
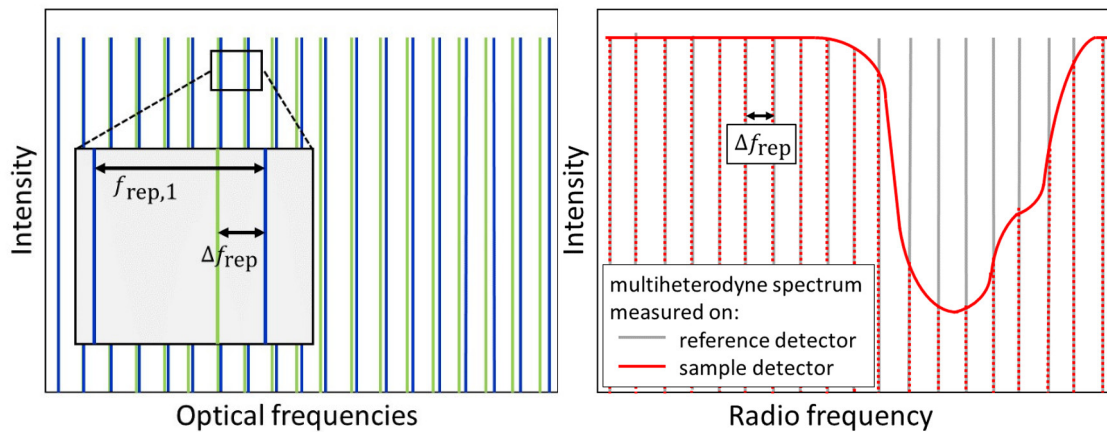

Fig. 2: Schematic of dual-comb spectroscopy based on the heterodyne of two frequency combs. Left: Two frequency combs with different frequencies in optical range. Right: Heterodyne spectrum.

2.3.   Quantum Cascade Lasers

A laser is a light emitting device through a process of optical amplification relying on the stimulated emission of electromagnetic radiation. The most common semiconductor laser is the diode laser. Diode lasers achieve stimulated emission through electron-hole recombination between the conduction and valance band. As a result, the emission wavelength is dependent upon the bandgap energy of the particular material. In contrast to this bandgap emission, a quantum cascade laser (QCL) operates based on intersubband transitions. As long ago as 1971, R.F. Kazarinov and R. A. Suris developed the theoretical concept for a QCL [11], but an actual experimental realization of an actual working QCL was first demonstrated in 1994 at Bell Labs in Murray Hill (New Jersey, USA) [12]. Since then QCLs were improved at a great pace regarding stability and accuracy.

A QCL consists of a series of stacked layers of varying semiconductor materials with different bandgaps. The nanometer-thick heterostructures are often based on GaAs and InP [12]. The alternating use of different material layers leads to the formation of quantum wells. Therefore, subbands are formed in the conduction band resulting in a decoupling of the emission wavelength from the bandgap energy. In the QCL, the stimulated emission is now achieved by quantum effects within the conduction band itself, as so-called intersubband transition. Instead of an electron-hole recombination between conduction and valence band
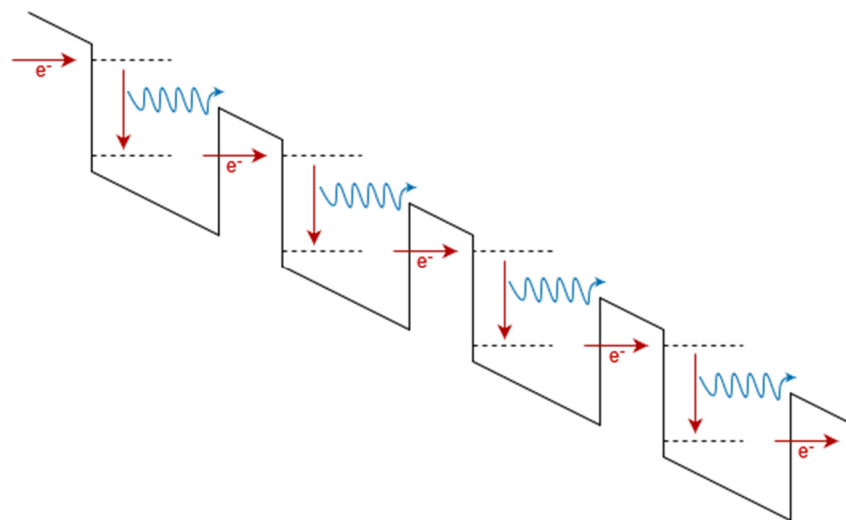
Fig. 3: Schematic for the intersubband structure of a QCL. An electron is traversing the quantum well structure while causing the emission of multiple photons.

like for conventional diode laser, the electron stays within the conduction band.

As schematically shown in **Fig. 3**, a cascade effect arises if a sloped potential is applied. Once an intersubband transition occurred and a photon was emitted, the electron can tunnel to the next period of the QCL structure where the process repeats. A single electron can cause the emission of multiple photons by moving along the quantum wells structure. The combination of quantum and cascade effects results in high output powers for a QCL.

In section 2.2, frequency combs were introduced as the emission products of a short-pulsed laser. In general, the emission of pulses is a sufficient condition for the generation of frequency combs but they are not necessary. Instead, the only requirement is the periodicity of the output waveform [13]. The phase-locking between modes is thus the necessary condition, leading to spectrum of modes that are spaced by f_{rep}. A representation of the phase-locking of different longitudinal modes of a laser is shown in **Fig. 1**. There are several methods for obtaining active and passive phase-locking of traditional lasers [7,13,14]. But together with their compactness and capability of on-chip integration, QCLs are attractive laser sources for direct mid-infrared radiation which is useful for spectroscopic applications and advantageous compared to traditional lasers [15], although other phase-locking mechanisms are necessary.

It was demonstrated that the phase-locked frequency comb operation in a QCL can be achieved with a four-wave mixing (FWM) process [16]. FWM is a third-order nonlinear process arising in QCLs. The FWM phenomenon involves three waves with frequencies ω_1, ω_2, ω_3 in a field that produce a forth frequency ω_4, which is due to energy conservation given by:

$$\omega_1 + \omega_3 = \omega_2 + \omega_4 \qquad (2.16)$$

And in the degenerate case, where two frequencies are equal, expressed by:

$$2\omega_2 = \omega_1 + \omega_3. \qquad (2.17)$$

By regarding a system of three oscillators as example, it can be understood how FWM is responsible for the creation of modes spaced equidistantly in frequency (see [7]). Provided that the oscillators at ω_1 and ω_2 are coupled through the FWM, they produce a new frequency at $\omega_3' = 2\omega_2 - \omega_1$ (**Fig. 4**). If ω_3' and ω_3 lie closely together, the generated

oscillator at ω_3' can act as a master oscillator and lock the frequency of the slave oscillator. This injection locking ($\omega_3' = \omega_3$) leads to the following spacing between the modes:

$$\Delta\omega_{23} = \omega_3 - \omega_2 = \omega_3' - \omega_2 = (2\omega_2 - \omega_1) - \omega_2 = \omega_2 - \omega_1 = \Delta\omega_{12}. \qquad (2.18)$$

In conclusion, FWM creates three equally spaced modes. Extending the simple system of three oscillators to a multimode system shows that the FWM process is able to injection lock the equidistant spacing for modes that originally exist in a system, therefore enabling the generation of a frequency comb. **Fig. 4** shows schematically this FWM as phase-locking mechanism for frequency comb generation in a QCL.
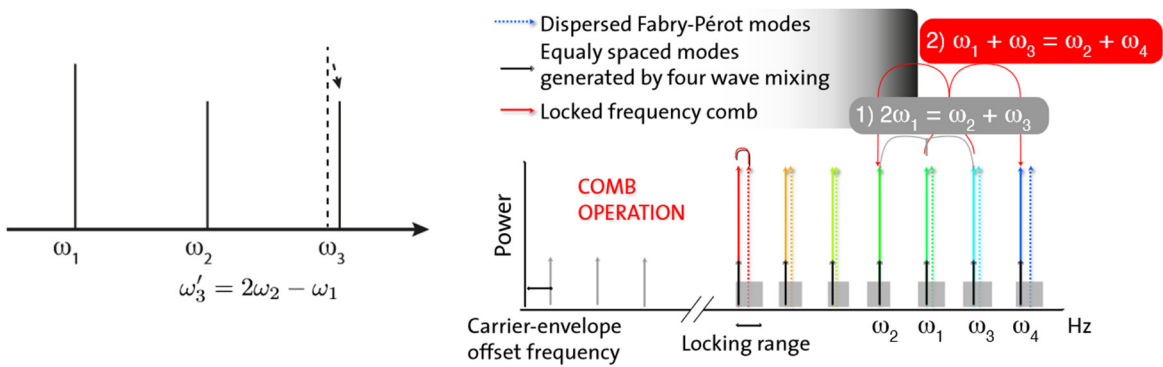
Fig. 4: Operation principle for a QCL comb. Left: Schematic of the FWM in three oscillator system. Right: The FWM generated equally spaced modes injection lock the original modes. Both figures adapted from [7].

2.4. NO and H₂O Absorption

As indicated in the introduction, both water and nitrogen oxides form during a hydrogen combustion process. When the combustion takes place in the stratosphere, the environment affects caused by the exhaust gases need to be regarded carefully. As a prerequisite, data on the temporal development of the amount of species that are formed need to be gained from experimental investigations such as the laser absorption spectroscopy.

An airbreathing hydrogen-fueled engine produces mainly water, with the overall reaction result given by [17,18]:

$$2\,H_2 + O_2 \leftrightarrow H_2O. \qquad (2.19)$$

The total reaction scheme involves various steps and was originally developed by Jachimowski [17].

The other byproduct from a hydrogen combustion engine are nitrogen oxides (NO_x). To create nitrogen oxides, a high local temperature and an excess of oxygen are needed, hence the oxidation of atmospheric nitrogen (N_2) leads to the formation of nitrogen oxides. Researches found nitric oxide (NO) as the main source for the NO_x emissions.

The most widely used model for the prediction of nitrogen oxide emissions is the extended Zeldovich model [19]. The model is based on the three following hypotheses [20]:

1) the source of NO_x is the atmospheric nitrogen
2) the thermal NO_x formation reactions are decoupled from the fuel oxidation process as the fuel oxidation reactions are fast in comparison to the NO_x formation reactions
3) the majority of nitrogen oxides resulting from the formation and reduction processes are NO molecules, in consequence the modelling of all NOx emissions is based only on this molecule

Here, the chemical mechanisms are restricted to the modelling of thermal NO, since the prompt NO reactions that only occur at low temperatures are neglected as high temperature dominate in the regions of the flame and in the postflame gases. Under these assumptions, the whole process is governed primarily by the three following reactions [20,21] :

$$N_2 + O \leftrightarrow N + NO \qquad (2.20)$$

$$N + O_2 \leftrightarrow NO + O \qquad (2.21)$$

$$N + OH \leftrightarrow NO + H \qquad (2.22)$$
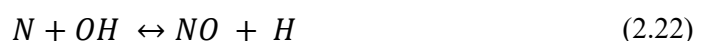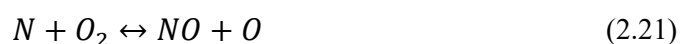
The first two reactions describe the oxidation of atmospheric nitrogen. The third equation was supplemented to extend the classical Zeldovich mechanism in order to account the influence of OH radicals forming during the combustion.

The reactions involve the O and OH radicals that are as well part of the fuel oxidation mechanism. But according to the second assumption, the thermal NO production is decoupled from the fuel oxidation and thus the NO formation rates are simply calculated by assuming equilibrium values for the temperature and the concentrations of O_2, N_2, O and OH [20]. The non-equilibrium effects on the NO formation rate are present on a wide

temperature range but only during the initial stages of reaction which are only responsible for a small part of the NO formation [20]. The total amount of formed NO depends on factors like the air/fuel ratio, the engine speed or the ignition timing [22].

Although the hydrogen combustion with air is advantageous regarding the absence of emitted carbon and sulphur (if the pre-production of liquid hydrogen is provided from renewable energy sources), it has to be considered that water as well as NO have an impact on the atmospheric system. The effects on atmospheric composition and the climate impact depend strongly on flight altitude [23,24].

The emissions of H_2O increase by a factor of at least 2.6 in comparison to those emitted by kerosene fueled flight vehicles [25]. Water vapor can cause partly a direct radiative impact on the climate system and indirectly lead to lower stratospheric temperatures resulting in the creation of more polar stratospheric clouds which influences the polar vortices [26]. Studies show that the influence of water vapor is rather small compared to other trace gases [25], but it has to be considered that the knowledge about feedback loops concerning the climate and Earth's atmosphere is limited at the moment and needs further research.

The influence of NO emissions on the climate is indirect through its chemical interaction with atmospheric ozone [27]. At altitudes below about 15 km, NO_x emissions are associated with an increase of the upper tropospheric ozone, hence strengthening of the greenhouse effect. But the NO_x increases coincidently the atmospheric OH concentration which in turn decreases the methane (CH_4) lifetime [28]. A lowered atmospheric CH_4 concentration reduces the greenhouse effect. NO_x emissions cause damage to plant life and may contribute to the problem of acid rain [28]. In the stratosphere at high altitudes (above about 15km), where the ozone density reaches its maximum, NO_x emissions cause the destruction of ozone [29]. Removal of O_3 from the stratosphere yields an increase of ground-level ultra-violet radiation, which might cause skin cancer and eye diseases [30]. Studies on the possible reduction of NO_x emission with simultaneous maintenance of the engine performance identified the equivalence ratio as a key parameter for NO_x formation [30].

A spectroscopic simulation for a hydrogen combustion at realistic conditions during supersonic wind tunnel experiments (p = 4.2 bar, T = 2300 K) is presented in **Fig. 5**. The theoretical spectra are simulated using HAPI, the programming interface of the HITRAN

molecular spectroscopic database [31,32]. As a mixture of direct observations and theoretical calculations resulting from quantum-mechanical solutions, the HITRAN database contains high-resolution line-by-line transmission values. While the figure on the right spans a larger region in the infrared region, the zoomed-in spectra on the right cover wavenumbers between 1720 cm^{-1} and 1760 cm^{-1} equivalent to the spectral coverage of the spectrometer used in this work. The absorption path length l corresponds to the width of the wind tunnel model, here chosen to be $l = 6.6$ cm as in a previous experimental campaign [3]. In this flow case, the absorption of NO and H_2O can be separated and is visible at the same order of magnitude. Thus, the reconstruction of the state of both species can be performed with only one coincident measurement.
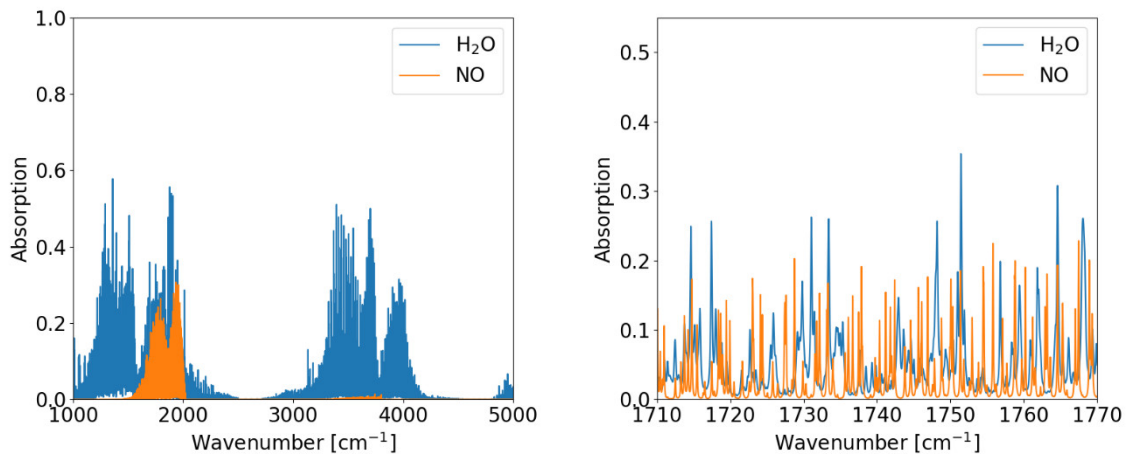
Fig. 5: Simulated NO and H_2O absorption spectra for a representative gas state during hydrogen combustion ($p = 4.2$ bar, $T = 2300$ K, $w_{H2O} = 0.08$, $w_{NO} = 0.03$, $l = 8$ cm) obtained using HITRAN/ HAPI. Left: Broad spectra. Right: Zoomed-in spectra to spectral coverage of used QCL lasers.

In the past decades, different work groups experimentally approached the detection of NO and H_2O in shock tube studies with various methods. An overview of their work will be shortly summarized in the following.

* A first application of the heterodyne laser absorption spectroscopy measurement system at the HEG was performed in 2020 [3]. The studied supersonic hydrogen combustion flow was generated inside the combustion unit of a small-scale wind tunnel model. This model is based on the waverider vehicle concept by ESA with three strut injectors that bring the hydrogen into the combustor. To allow optical

access, several infrared-transparent window ports were mounted to the model. The laser was coupled out of the spectrometer with fibers. By installing optical couplers to the model in front of the windows, the laser was coupled into the model and thus allowed line of sight measurements perpendicular to the flow. A challenge for the application of any optical measurement technique in facilities like the HEG is the limitation of available test time to around 5 ms.

It was possible to demonstrate the general ability to employ the laser absorption spectroscopy for multi-species measurements at high acquisition rates. But the results are rather only relative and differed depending on the used measurement mode and post-processing methods. This raises the need for more extensive calibration measurements and a detailed look on both the influence of different measurement modes on accuracy and the influence of outer circumstances like for example the coupling fibers that are sensitive to little disturbances.

* In 1996, Mohamed et al. experimentally detected NO in the F4 high-enthalpy hypersonic wind tunnel at ONERA (France) by applying tunable diode laser absorption spectroscopy (TDLAS) for flow diagnostics [33]. Here, NO is produced from the arc chamber and remains in the hypersonic flow, thus implying it can be measured after the expanding nozzle in the free stream. The study's goal was to test the feasibility on measuring freestream velocity, temperature, and NO concentration based on the absorption of NO. The build spectrometer works in the mid-infrared range and was shown to be suitable for NO detection. The absorption of NO was especially proven to be successful regarding nonintrusive velocity measurements. The measurements of temperature and NO concentration were less useful as absorption in the boundary layers led to significant systematic errors in the inferred values. For that, the authors suggested the use of two laser beams probing two different rotational states. Another challenge was the amount of noise in the experimental data. As consequence, the analysis based on the least-squares method resulted in low precision because of outlying points. Future work on improving the analysis algorithm with a non-least-squares fitting was intended.

* In 1971, Bowman presented the results of an experimental and analytical investigation of NO formation during the shock-induced combustion of hydrogen-oxygen-nitrogen mixtures to determine the mechanism for NO formation during the combustion [34]. The concentration-time histories of the gas species were measured with spectroscopic techniques. While the NO concentration was measured by monitoring the absorption of ultraviolet radiation by the molecules, the H_2O concentration was obtained by monitoring infrared emission. Bowman set up a complex optical system. The infrared radiation passes through collimating slits and is focused on an Au-Ge detector, whose output signal was amplified and displayed on an oscilloscope. To eliminate atmospheric absorption, the infrared optical system was enclosed in a housing which is purged with nitrogen. The UV radiation from a Xe/Hg lamp was focused into a narrow beam to pass through the shock tube test section. The beam was then focused on a photomultiplier-equipped monochromator from where the signal was displayed on an oscilloscope. Both techniques had a quite high temporal resolution in the µs-range, but the NO concentration was only measured at one vibrational state. However, Bowman concluded that the observed NO formation rates are consistent with a two-reaction mechanism for nitrogen chemistry.

* In 2016, Almodovar et al. used a pair of quantum cascade lasers in the mid-infrared near 5 µm probe rovibrational transitions in nitric oxide's fundamental band at high temperatures [35]. The line parameters of the selected transitions, including line strengths and collision broadening coefficients of nitric oxide with argon and nitrogen, were evaluated during controlled room-temperature static cell experiments and high-temperature shock tube experiments at temperatures between $T = 1000$ and 3000 K, and pressures between $p = 1$ and 5 atm. The quantitative two-color temperature sensing strategy was demonstrated in non-reactive shock tube experiments from $T = 1000$ to 3000 K to validate thermometry and during a nitric oxide formation experiment near $T = 1700$ K and $p = 4$ atm to highlight capability for temporally-resolved species measurements at MHz rates. While the first laser probed the transitions at 1940 cm^{-1}, the second laser measured the transitions near 1987 cm^{-1} by modulating the output wavelength.

* In 2021, Girard et al. [36] report on their first try to TDLAS for measurements of freestream NO rotational and vibrational temperatures and partial pressures, collected in the Caltech T5 reflected shock tunnel with test times on the order of 1 ms. Th authors state "the goal of these and future experiments is to develop and demonstrate TDLAS experimental strategies for high-enthalpy impulse facilities". They used in total three QCLS targeting NO with a minimal spectral spacing of 0.2 cm^{-1}. The raw data collected during the experiments were converted into integrated absorbance time histories by computationally fitting the transition absorbances to a Voigt lineshape model. They observed qualitatively good agreement between the measured and simulated data, showing similar trends in decreasing temperature and partial pressure. Future work aims to improve the measurements to get a more quantitative comparison.

* In his PhD thesis submitted in 2017, Wheatley investigated the application of TDLAS for water vapor sensing during scramjet experiments at the X3 super-orbital expansion tunnel at the University of Queensland [37]. He labels the TDLAs technique as of high potential, but the performed experiments revealed some difficulties. As the TDLAS system was placed outside the dump tank, so the signals were detected external, the external water vapor led to parasitic absorption signals. The use of fiber optics is suggested. Other difficulties with the regard to the measurement technique were the determination of the exact modulation frequency for the lasers, which complicates the reconstruction of spectra, as well as a lack of intensity calibration of the system.

3. Experimental Apparatus

The main instrument is the mid-infrared spectrometer whose components and operating principle are explained in greater depth in this section. The different possible measurement modes are presented.

This chapter describes the setup including all structural components. The test procedures for different installation configurations of a Herriott cell are explained immediately following the respective setup description.
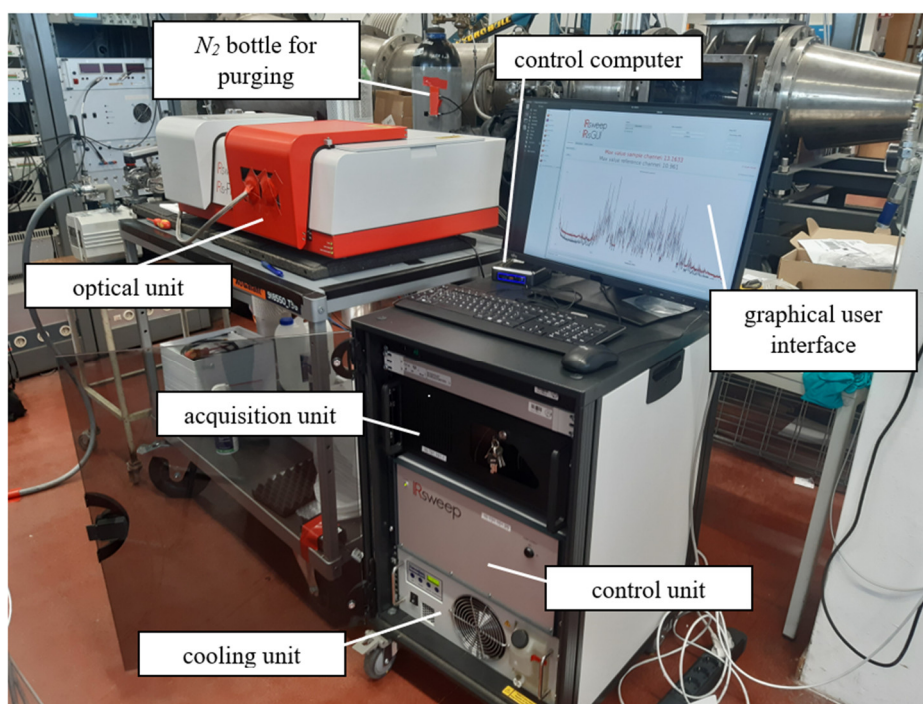
Fig. 6: Components of spectrometer set-up.

3.1.   The Spectrometer

The IRis-F1 spectrometer by the Swiss company IRsweep operates at a narrow wavenumber range. The special feature of this spectrometer is its replaceable laser PCB module. Each laser module offers a different wavenumber regime that can be used to detect different gases. In this case, the module has a central wavenumber of 1740 cm^{-1} and covers a spectral region of 40 cm^{-1}, enabling measurements for a wavelength at $\lambda = 5.8\ \mu$m.

The whole set-up consists of the optical unit as main element, an acquisition unit, the laser control unit, a water chiller and a control computer. These components are shown on a photograph in **Fig. 6**. The optical unit is the main element of the spectrometer where the measurements with a sample are performed. **Fig. 7** presents a schematic top view of the optical unit where the beam paths are sketched.
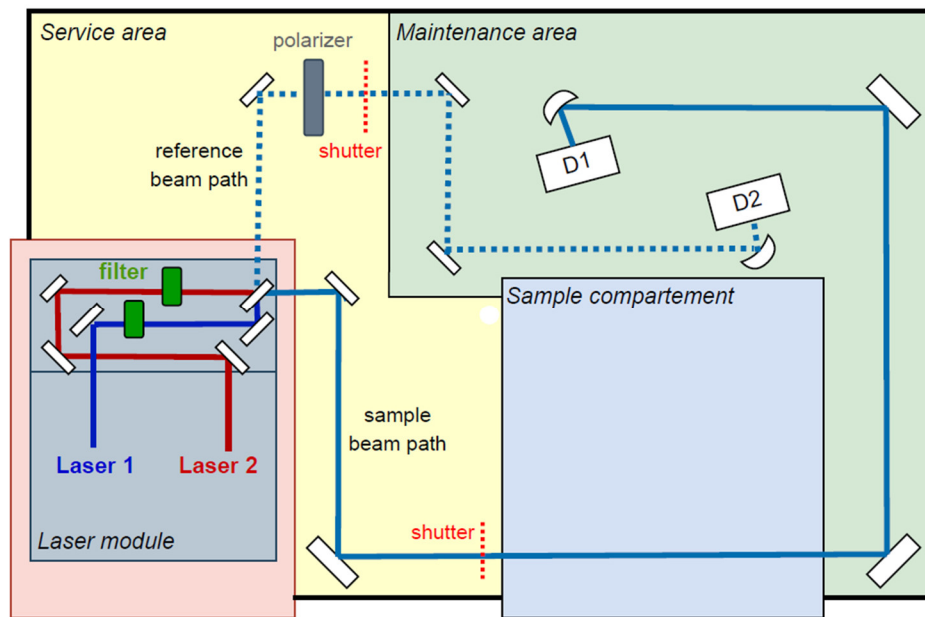
Fig. 7: Schematic top view of the spectrometer's optical unit including the beam paths. The sample beam (solid) traverses the sample compartment and gets attenuated while the reference beam (dotted) reaches the detector undisturbed.

The laser infrared radiation source is the laser module that contains two QCLs. Both lasers are controlled separately by the control unit. The laser module is continuously cooled via coolant connectors from the chiller unit to ensure a stable operation of the QCLs. The aperture for each laser can be blocked with a shutter. Behind the apertures of the laser module, the two beams from laser 1 and laser 2 are mitigated through filters and then combined through a beam-splitter. The system now separates in two different beam paths. This method is called amplitude-sensitive configuration (ASC).

The reference beam does not interact with a sample and reaches the reference detector unaltered. A polarizer adjuster can regulate the laser radiation power of the beam. The other path guides the so-called sample beam into the sample compartment. Here, the beam can be

manipulated by placing optical accessories and a sample on the breadboard of the sample compartment. It is as well possible to guide the beam out of the sample compartment, which will be the case for external measurements described in later section. After the transmission through the desired destination, the beam is guided back into the sample compartment. Subsequent to the sample compartment, plain mirrors lead the sample beam on a parabolic mirror that focusses the beam onto the sample detector. The mirrors are fine-adjustable to align the beam optimally.

The detectors record the heterodyne resulting from the combination of the two lasers. Afterwards, the undisturbed reference path and the sample path are compared to study the influence of the sample on the beam. It is necessary to also cool the detectors during their operation.

The control unit drives current and temperature for the lasers. Optimal initial parameters are listed in **Table 1**. Starting from these parameters on, small variations in the order of $0.01°C$ and $0.1mA$ may need to be done in order to optimize the signal. The control unit communicates with the control computer via an ethernet connection.

Table 1: Initial parameters for the lasers.

	Current [mA]	Temperature [°C]
Laser 1	835.9	-8.85
Laser 2	899.2	-13.25

The acquisition unit is a computer that enables communication with the control unit and the optical unit via an ethernet connection and processes and stores all the measured data from the detectors on the optical unit. It contains the high bandwidth acquisition electronics and data evaluation algorithms to transform the time-domain data into spectral data. A graphical user interface to access this is provided by the control computer. It enables to control all relevant parameters like the operating conditions for the lasers or the measurement data.
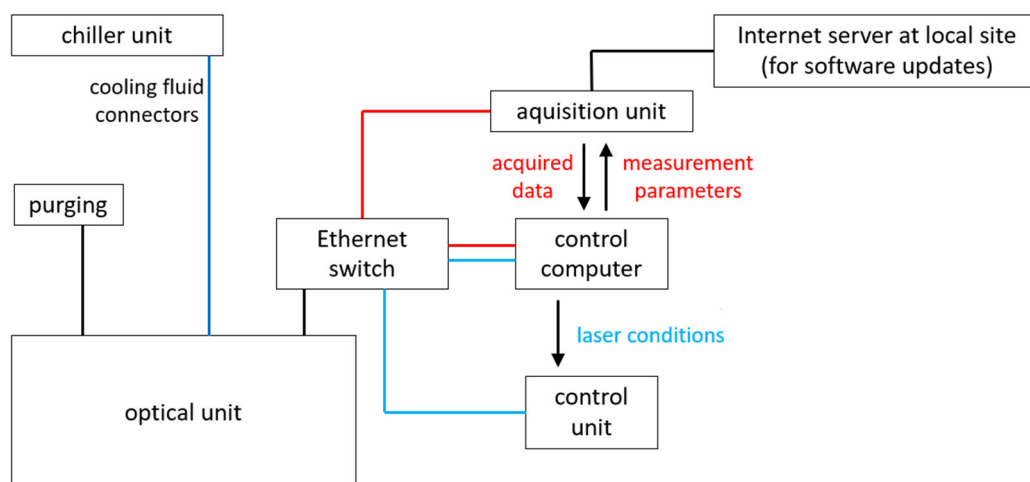
Fig. 8: Connections of the whole spectrometer system.
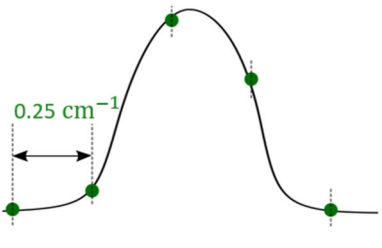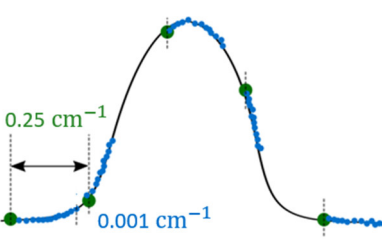
All ethernet and other cable connections between the different components of the IRis-F1 are presented in **Fig. 8**. The figure also shows a connection for purging of the optical unit. During a measurement, the whole device is purged with N_2 for removing ambient air and especially water molecules that might disturb the measurement. N_2 has very weak absorption in the investigated infrared regime and thus is suitable as purging gas.

As stated above, the measurements are controlled either by the graphical user interface on the control computer or via a python client. A typical measurement procedure consists of a transfer, background and sample measurement. A transfer is taken by closing all shutters for receiving the left signal on both detectors. The transfer function describes the electronic noise of the system when there is no light on the detectors. With the reopened shutters but without the sample gas, a background measurement is carried out. The number of acquisitions for averaging the background spectrum can be chosen. Then, the sample is measured. The data can either be saved as single spectra or be averaged over several acquisitions. The background is stored after being recorded for the first time. Despite that, it is recommended to take a background every time just shortly before the sample is measured.

3.2. Measurement Modes

Table 2: Overview about possible measurement modes.

spectrum	static mode	time resolved mode
constant lasers	**LongTerm** single spectrum from averaging over multiple number of measurements	**TimeResolved** multiple measurements yield a spectrum for each time instant (acquisition each 4 µs)
modulated lasers	**StepSweeping** single spectrum from averaging multiple number of measurements with step-wise tuning of current	**FastSweeping** multiple measurements yield a spectrum for each time instant (1 ms), periodical modulation of laser current in a saw-tooth wave

The spectrometer allows four different measurement modes: *LongTerm, TimeResolved, Step-Sweeping* and *FastSweeping*. **Table 2** shows a short overview on these opportunities.

In *LongTerm* mode, a single spectrum is obtained from averaging multiple number of measurements. In *TimeResolved* mode, multiple measurements are taken, yielding a
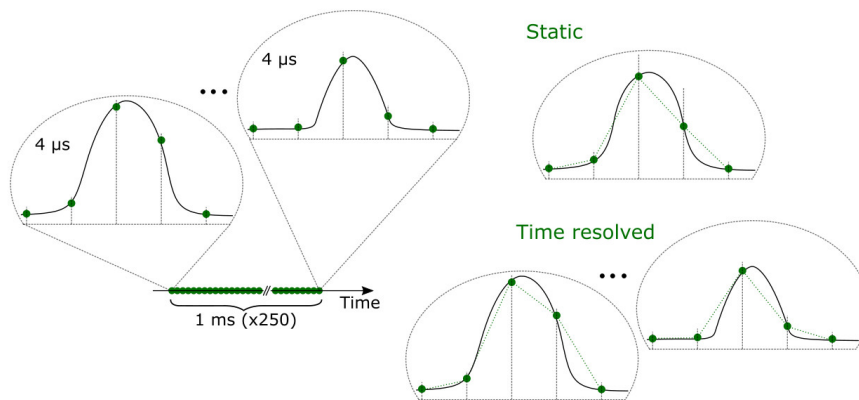
Fig. 9: Exemplarily difference between *LongTerm* and *TimeResolved* measurement modes.

spectrum for each time instant. Both these modes leave the lasers current and temperature constant throughout the acquisition allowing time resolutions at 4 μs and a spectral point spacing of 0.3 cm^{-1}. For an exemplifying acquisition length of t_{aq}= 1 ms, all the 250 acquisitions are averaged for *LongTerm* mode into one single spectrum while each of the 250 acquisitions is saved separately in *TimeResolved* mode (**Fig. 9**). But the given point spacing between adjacent lines is generally too large to sample all narrow absorption features of molecular gases sufficiently. Especially the precise determination of gas concentrations based on the absorption features is complicated by a large point spacing if not all features can be resolved appropriately.

The tuning of the QCL frequency combs' emission frequencies via temperature and current reduces the gaps between adjacent lines. By alternately and stepwise increasing the current of both lasers in *StepSweeping* mode, the gaps between points are closed without moving the multiheterodyne beat note to frequencies outside the detection bandwidth. The schematic procedure is shown in **Fig. 10**. To prevent possible QCL mode switches during operation that change the form of the heterodyne, or the generation of subcombs due to a too large current tuning range, it is necessary to define a suitable current ramp consisting of stepwise tuning of the currents. By sweeping through this ramp at different temperatures, the gap is filled. The recommended stabilization times for current and temperature steps are
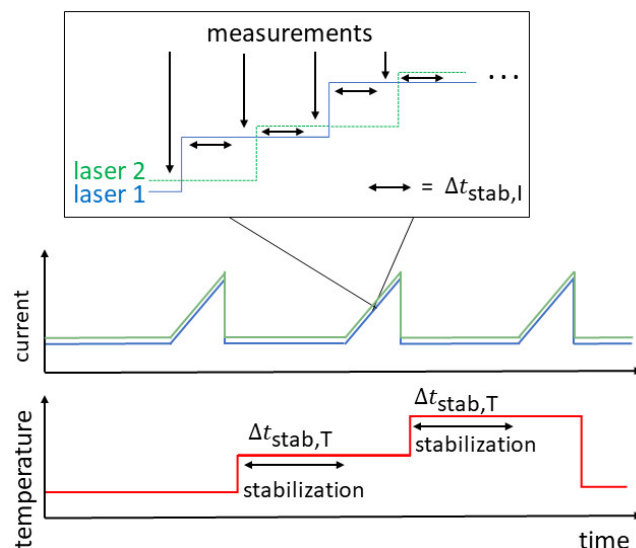
Fig. 10: Illustration of the StepSweeping technique involving stepwise tuning of current at different temperatures.

$\Delta t_{\text{stab,I}} = 1$ s and $\Delta t_{\text{stab,T}} = 60$ s, respectively. This method decreases the spectral point spacing to $2 \cdot 10^{-3}$ cm^{-1}.

In *FastSweeping* mode, the current of the lasers is periodically modulated in a saw-tooth wave at a rate of 5 mA/V using a wave generator (**Fig. 11**). Each ramp is set to increase from 0 V to approximately 6 V. A whole ramp is swept through in about 1 ms. The ramps are recorded, hence the frequency changes can be precisely reconstructed in the post processing. While the time resolution of the measurements decreases by this method, it increases the spectral resolution by a factor of almost 250. This is a theoretical value when sampling with 4 μs during 1 ms that was checked experimentally in earlier measurements as well [3].
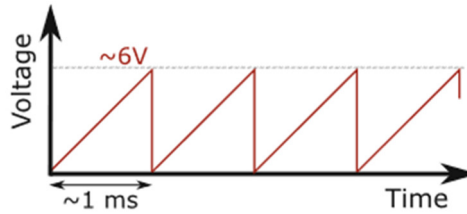
Fig. 11: Saw-tooth wave generator output to modulate current for *FastSweeping*.

3.3. Herriott Cell
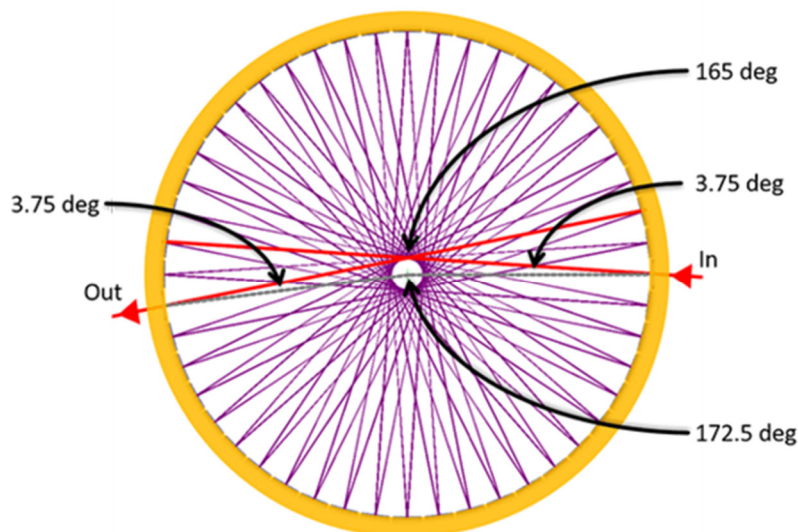
Fig. 12: Schematic of a circular-shaped Herriott cell (IRcell-S4 [16]).

In order to perform calibrations with an increased sensitivity for the optical measurement, it is important to achieve a rather long path length within a compact setup. This can be realized with long-optical-path absorption cells, usually referred to as Herriott cells [38]. Such cells are regularly used for gas phase spectroscopy of trace species in several applications, e.g. environmental air quality [39,40] or breath analysis [41].

A Herriott cell is a multipass absorption cell. Each Herriott cell has angled optical ports that aid alignment into the cell. Main component of Herriott cells are mirrors that reflect a light beam several times to increase the path length before coupling the beam out again.

The cell used in the present scope of work is the IRcell-S that enables a path length of four meters [42,43]. The IRcell-S has a circular design. It consists of a series of individually curved mirror segments. **Fig. 12** includes a schematic for the beam path inside the Herriott cell. The cell offers two separate ports for coupling light in and out. The incoming beam is aligned to hit the second closest mirror counter-clockwise to the out-coupling port. The beam is then reflected by the mirror in a way that it hits each of the 46 mirrors centrally, producing a star-shaped beam. The beam exits through the exit aperture.
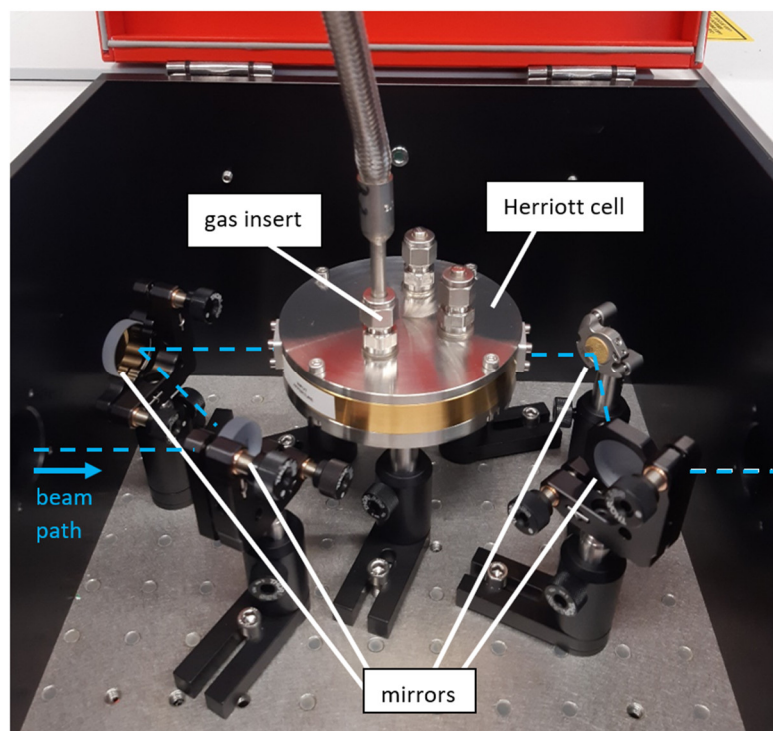
Fig. 13: The Herriott cell installed inside the sample compartment. Mirrors align the beam (dotted blue line) into cell and back on track towards detector.

Several additional optical elements are required to enable the coupling of the light beam in and out the cell. As shown in **Fig. 13** on both sides two mirrors are needed. They are necessary to align the beam and focus on the mirrors inside the cell. Since adjustment with infrared beams is inconvenient, the optics are aligned with the help of a red laser inside the spectrometer (**Fig. 14**). Prior to the sample compartment, the red laser is adjusted to be exactly in line with the infrared beam. The first two mirrors are first coarsely positioned. Then they are finely adjusted so that the red beam is visible in the center of each mirror inside the Herriott cell and the beam exits at the output aperture. Next the last two mirrors bring the beam back on the usual track.

The cell comes with three gas ports that can be used to either evacuate the cell's inside volume with a vacuum pump or to insert specific gas at different pressures. In this work, only one port is used as described in the section 3.4. The unnecessary ports are closed with a cap. According to the company IRsweep, the leak rate is about $6.68 \cdot 10^{-8}$ bar $\cdot$ L/s.
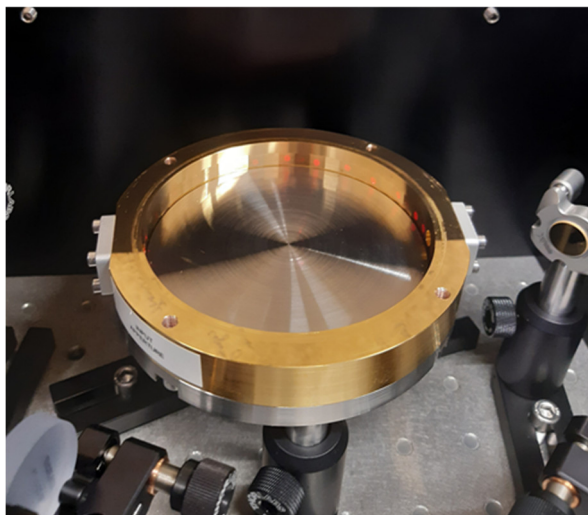
Fig. 14: A red laser helps to align the Herriott cell.

3.4. Experimental Details
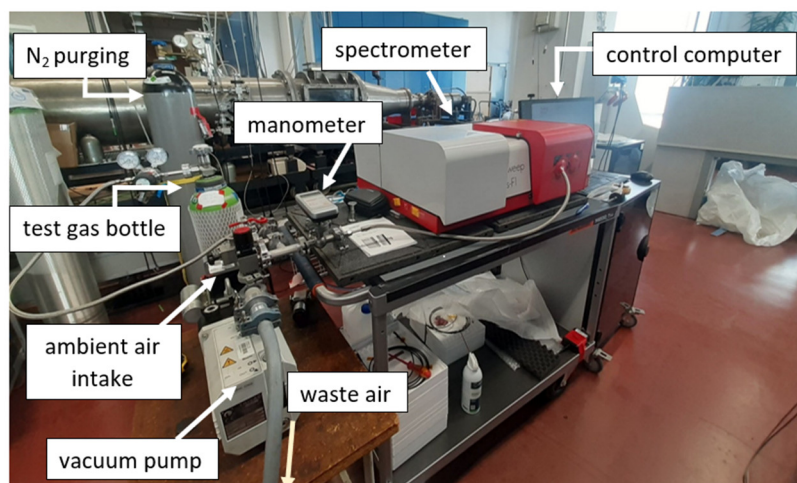
Fig. 15: Experimental set-up with the internal placed Herriott cell.

At the beginning, the Herriott cell is placed inside the spectrometer's sample compartment. The whole set-up is shown in **Fig. 15**. The cell is connected to a gas system that consists of a vacuum pump to evacuate the cell and different valves corresponding to insertable test gases. Preliminary measurements showed the necessity to use flexible stainless-steel tubes (**Fig. 16** left) as the earlier used plastic tubings were slightly permeable for water from ambient air. The cell is evacuated prior to experiments. During experiments, the cell is filled

with gaseous mixtures at different pressures $p = [100, 300, 500, 700, 900]$ mbar.
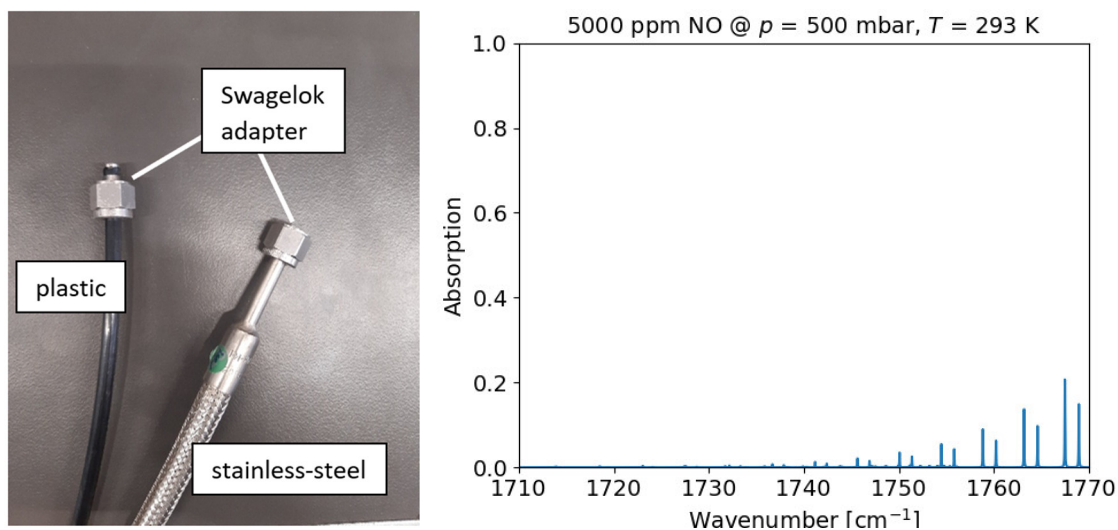
Fig. 16: Left: Plastic and stainless-steel tubings. Right: Absorption features of NO (5000 ppm in N_2) at room temperature are rather weak.

NO is not optimal for the calibration measurements as it is only weakly absorbing at room temperature (**Fig. 16** right). Despite that, a single measurement is reported in the results section. Instead, nitrous oxide (N_2O, known as laughing gas) and water from ambient air are used as calibration gases. The water content is calculated based on the measured room temperature and relative humidity. For each pressure and gas combination, a measurement in *LongTerm* and *StepSweeping* mode is carried out. In *StepSweeping* mode, a total of 328 tuning steps are defined. The *StepSweeping* requires an external triggering source that is realized with a relay board. Access to that is possible with a python communication script. The trigger signals are led directly to the control unit. The current and temperature measurement parameters are listed in the appendix. To understand why the *StepSweeping* mode requires stabilization times and which influence that may have on the measurement quality, the current stabilization time in *StepSweeping* measurements is reduced in a series of measurements that spans five orders of magnitude including $\Delta t_{\text{stab,I}} = [1, 0.1, 0.01, 0.001, 0.0001, 0.00001]$ s. The temperature stabilization time remains at $\Delta t_{\text{stab,T}} = 60$ s because in *FastSweeping* only the current is modulated. The smallest current stabilization time $\Delta t_{\text{stab,I}} = 0.00001$ s corresponds to just about the time scale for the periodic modulated

current.
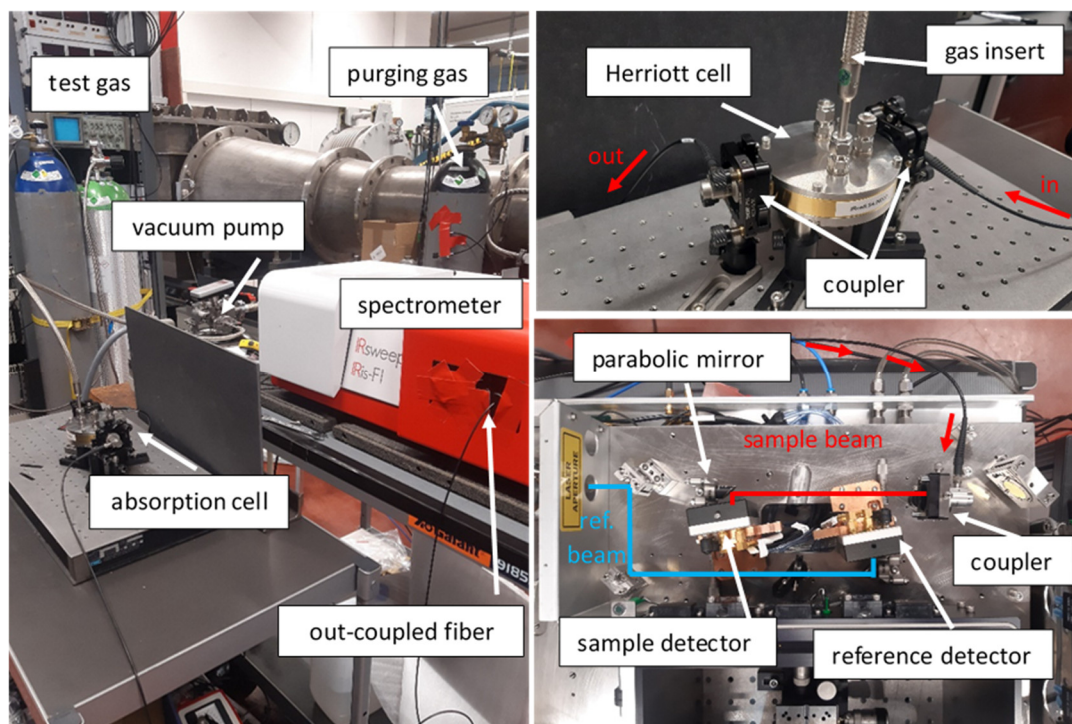
Fig. 17: Details on external set-up. Left: Overview. Top right: Herriott cell and two couplers placed on additional breadboard. Bottom right: Coupler installed to align the fiber beam onto the sample detector.

Afterwards, the Herriott cell is removed from the sample compartment and installed on an external breadboard as shown in **Fig. 17**. This application requires the use of optical fibers and additional optics. The optical setup coupling the sample beam out of the spectrometer consists of a lens which focuses the light onto an optical fiber with an FC/B connector at Brewster angle (IRflex IRF-Se-12, **Fig. 18**). The fiber is based on chalcogenide glass (As_2S_3). Due to the high refractive index of this material (~2.4 for As_2S_3), there are high reflections caused at the entrance and exit around 17%. The FC/B connector is polished at a specific angle that allows the incident light beam to enter at the Brewster angle. The Brewster angle minimizes the back reflections and maximizes the power being coupled into the fiber.

The other end of the fiber transporting the light to the external Herriott cell has a SMA connector (**Fig. 18** left) inserted on a fiber coupler (Thorlabs RC02SMA-P01). Such a coupler consists of a kinematic mount and the SMA-connectorized collimator, as shown in **Fig. 19**. The coupler is used to align the beam into the Herriott cell. A second coupler receives

the beam after it passed the cell and guides it to a second fiber, which is then coupled again on a third coupler. This one is installed in the spectrometer's maintenance area and is aligned with the parabolic mirror inside of the spectrometer to guide the incident beam directly on the sample detector (**Fig. 17**). The fibers used in this work have a core size of 12 μm and lengths of 2 and 3 meters.
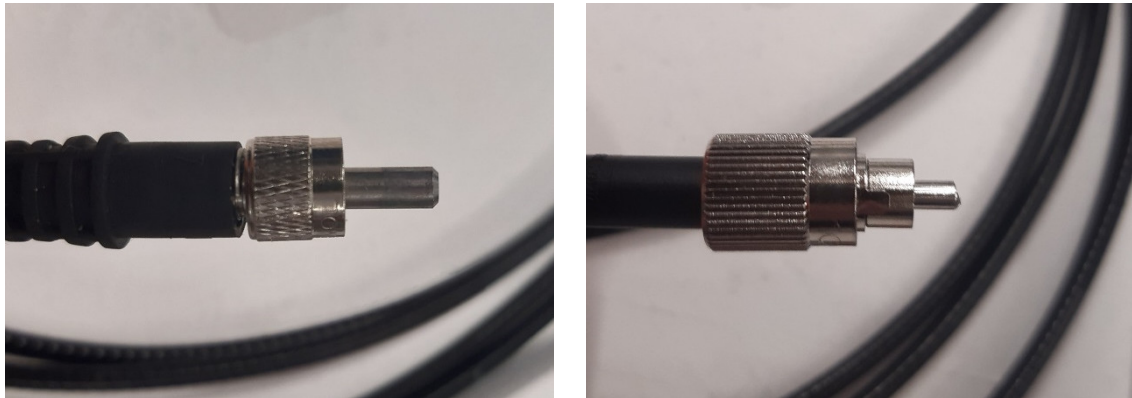
Fig. 18: Fibers with SMA connector (left) and with FC/B polished angle (right).
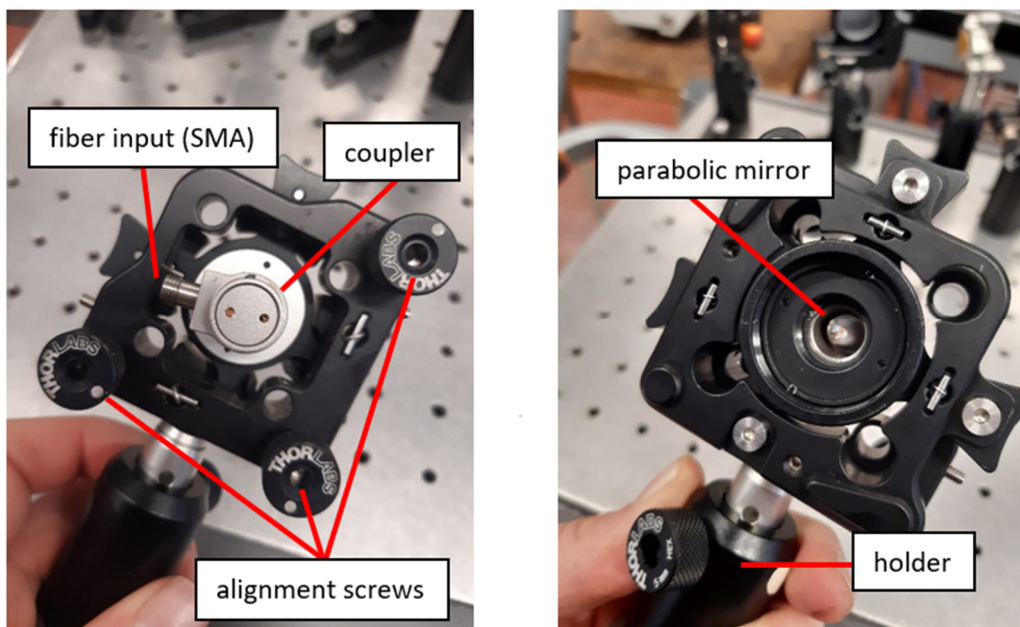
Fig. 19: Fiber couplers consisting of kinematic mounts and SMA-connectorized collimator.

The alignment procedure especially of the lens and the FC connector for the outcoupling requires high precision as maximum power is essential and back reflections at the entrance of the fiber need to be optimally prevented. The lens is plano-convex and creates a focal point at a distance of around 12 mm. The end of the polished FC/B connector needs to be

placed exactly in the focal point. For the adjustment, the holder for FC/B connector is installed on a three-axis nanopositioning stage (Thorlabs MBT616, **Fig. 20**). The three actuators are first used for coarse and later fine adjustment in micrometer drives. To find the optimal position, the fiber is guided to a detector connected to an optical power meter (Thorlabs PM100A). The detector is placed on the cold breadboard to prevent warming by other sources (**Fig. 20**).
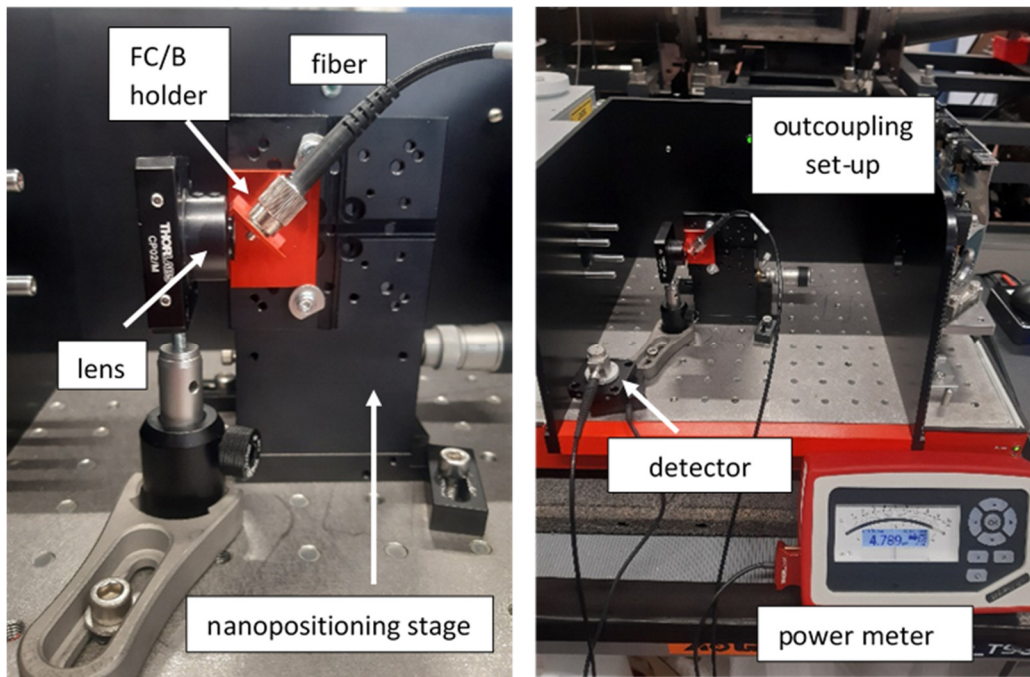
Fig. 20: Set-up for outcoupling of the beam for external use. Left: The beam is focussed on the fiber in Brewster angle. Right: A power meter is used to optimize the fiber position for maximal output.

The beam of each QCL is attenuated with 50% transmission (0.3 optical density) neutral density (ND) filters (Thorlabs ND06A) for the external application and 10 % transmission (1.0 optical density) ND filters (Thorlabs ND10A) for the internal use.

A parameter hinting at the quality of the measurement is the fallback rate. The fallback rate is automatically calculated in the processor of the spectrometer. A value between 0 and 100 is assigned for each acquisition. Every laser module has a unique range of fallback rate values that indicate normal operation. Among other things, it depends on the spectral distribution of the laser module at current conditions, the current power setting, the position

of the heterodyne signal recorded on the digitizer, the acquisition length of the measurement and the stability of the current laser conditions. Due to that, the absolute value of the fallback rate does not have a physical meaning, but a constant fallback rate indicates stable conditions. So instead of visually inspecting the fallback rate, it is an easier approach to see if something is wrong if the fallback rate under a known set of conditions deviates from the usual characteristic values. A very high fallback rate (> 60) is associated with problems due to the laser conditions, so it can be deduced that the laser conditions need to be improved. If the fallback rate is highly fluctuating, this indicated a general problem with the signal, like for example the appearance of subcombs, the broadening of heterodyne lines or a changing shape of the heterodyne signal.

With this external set-up, the *StepSweeping* tests are exactly repeated as in the internal set-up to study the influence of the fibers. For the sake of completeness, it should be briefly mentioned the *FastSweeping* measurement mode requires a different PCB laser module. It is driven by an external modified control unit. Additionally, an external wave generator creates the periodic modulation of the current. But due to limited time, the *FastSweeping* mode was not tested in the scope of this work.

4. Results

The data recorded with the acquisition card are processed automatically to generate HDF5 files readable by the python post-processing scripts. The file contains the transmission data as well as the measurement parameters. For further post-processing, specific python packages (provided by IRsweep) are used to analyze the data dependent on the used measurement mode. An important step in the processing is the manual wavenumber axis calibration.

First, this section describes the references taken for the wavenumber calibration procedure, followed by the technical requirements derived from measurements during the thesis work. Finally, results from the measurements with different configurations are presented.

4.1. Wavenumber Axis Calibration

The measured transmission data are corresponding to a wavenumber axis. At first, the processing software only guesses initially the present wavenumber axis based on the laser module settings. The wavenumber spacing is determined from an electronic characterization of the lasers, which is performed by the spectrometer's manufacturer and the information about the spacing is built into each laser module. Thereby, the wavenumber spacing is correctly calculated automatically, whereas the correct absolute wavenumber positioning is unknown. The calibration for that is done by aligning to a reference spectrum. The custom calibration references are created with HAPI, the programming interface of the HITRAN database [31]. By inserting substance species, concentration, pressure and temperature, the database outputs the transmission for a defined wavenumber range. It is as well possible to enter mixtures of any species to calculate the expected spectra on the defined conditions. Given both reference and sample transmission data, the spectra are plotted together. While the uncalibrated sample wavenumber axis is shifted manually, one tries to match the spectra as best as possible, in particular by orientating at the strongest visible features. Depending on the direction of recording from low to high wavenumbers or reversed, the obtained spectra may be flipped, arising the need to reverse the whole wavenumber axis during the calibration procedure. Once the calibration of wavenumber axis is optimized, it can be used as a reference for calibrating the wavenumber axis of other measurements with same laser

conditions. A new axis calibration is crucial as soon as the spectral signature changes, meaning a changed heterodyne signal or other laser operating conditions require an update of the axis. In the scope of this work, the HITRAN reference spectra are not only used for the wavenumber axis reference but especially to compare experiments with well-known parameters to the expected reference. In the following, we will no longer refer to transmission but to absorption spectra, obtained by subtracting the transmission values from 1 (= 100%).
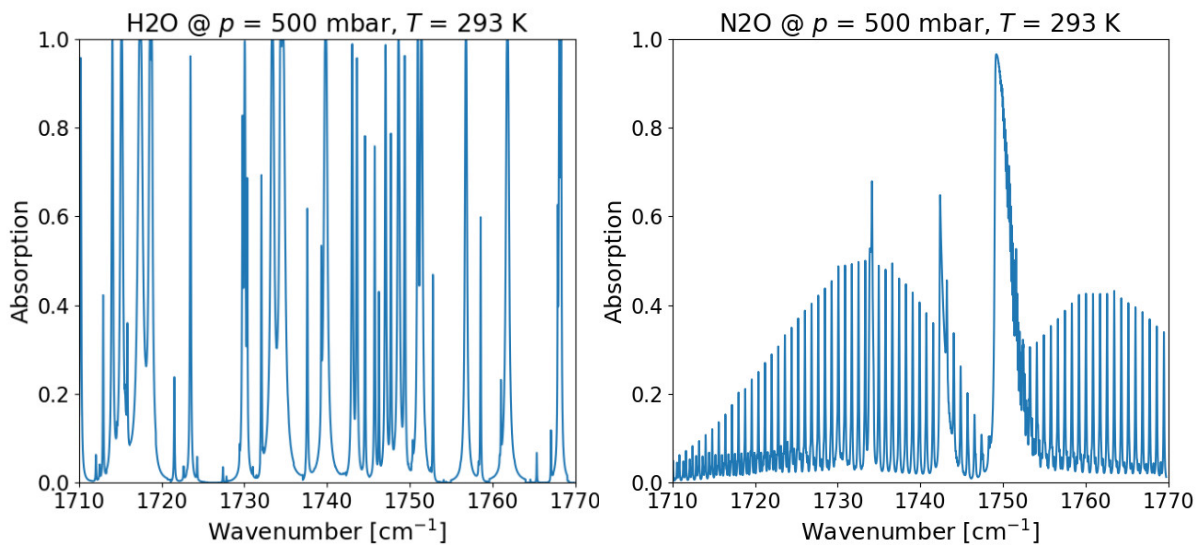
Fig. 21: Both N_2O and H_2O have strong absorption features at room temperature in the 4 m long path through the Herriott cell (p = 500 mbar). Data simulated with HITRAN.

Simulated example reference spectra for H_2O and N_2O are shown in **Fig. 21**. The path length is set to l = 4 m as the Herriott cell causes this elongation. The water concentration was calculated based on measured temperature and relative humidity of the ambient air (here: T = 20 °C, RH = 45 %, w = 0.00649% = 6490 ppm), whereas the used N_2O is assumed to be pure, so w = 100% = 10^6 ppm. Both spectra reveal characteristic absorption features. The N_2O spectrum is specifically marked by many sharp spectral peaks distanced by ~ 0.8 cm^{-1} with varying amplitudes. The strongest absorption peak is located at υ = 1749.2 cm^{-1}. Contrary to the sharpness of the other peaks, this peak is broadened. The H_2O spectrum features less peaks compared to the N_2O spectrum. But the majority of peaks corresponds to very strong absorption of nearly 100%. The form of the peaks differs, thereby enabling a good identification for the wavenumber axis calibration.

4.2. Technical Requirements for Calibration Measurements

While the experiments were conducted, several problems and challenges of various kinds occurred at different steps. By that, the tests revealed gradually the requirements necessary for the successful operation of calibration measurements but as well for operation in the external configuration with the fiber optics, which is crucial for wind tunnel experiments at the HEG. These points were part-wise already mentioned during the description of the set-up (chapter 3) but will be elaborated a bit further in the following.

- Tubing for gas insert

    Beginning with NO measurements, the obtained absorption spectra always didn't look as expected. The absorption features of any measurement were dominated by water absorption. To avoid more tests than necessary with the potentially dangerous NO, it was replaced with almost non-absorbing Helium with the aim to find the source of the error causing the parasitic water. As shown in **Fig. 22**, the disturbances are dependent on pressure of the inserted gas, meaning the more of a species is inserted to the cell, the more water is present. Here, the NO measurement ($p = 500$ mbar) strongly resembles an earlier measurement with 500 mbar inserted ambient air containing water. The error tracking covered first a check of the used valves. But changing them and rearranging the gas connections didn't change the results. For testing the hypothesis that the tubings are responsible for this behavior, the plastic tubings were replaced with flexible stainless-steel tubings between gas reservoir, the gas regulating system and the Herriott cell. Indeed, the plastic tubings caused the water addition. **Fig. 23** shows the impact of the changed tubings as the they drastically reduce the strength of absorption by water. An exact explanation for that cannot be given, but a permeability of the tubings for water vapor seems to be existing.
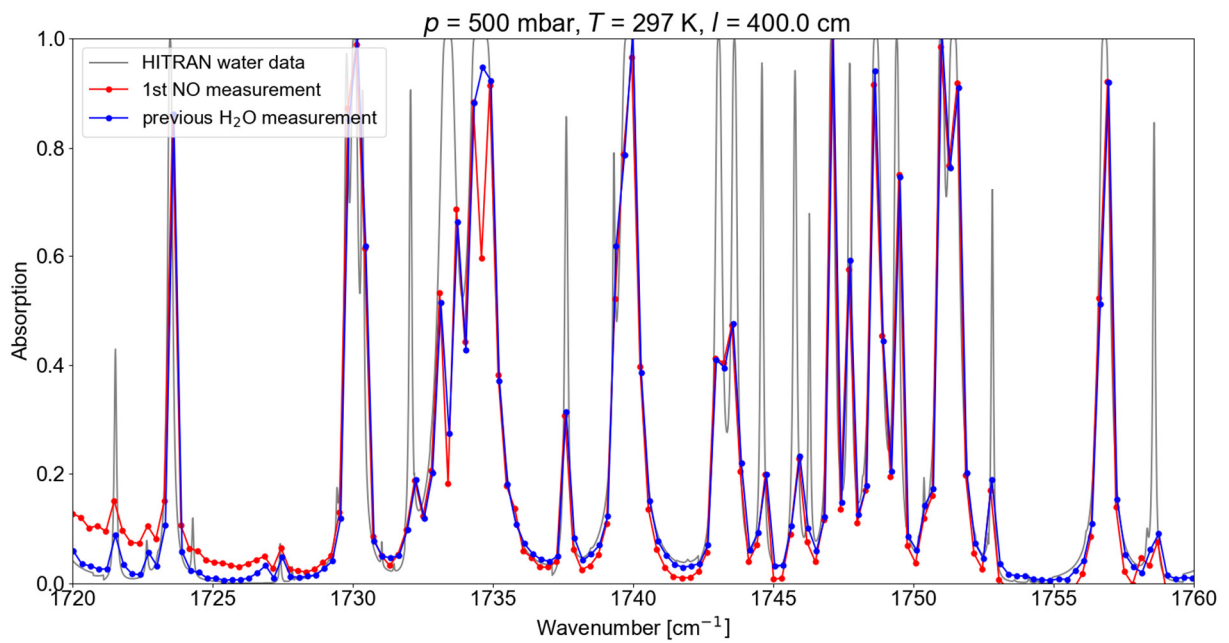
Fig. 22: Parasitic water content destroys the measurement.
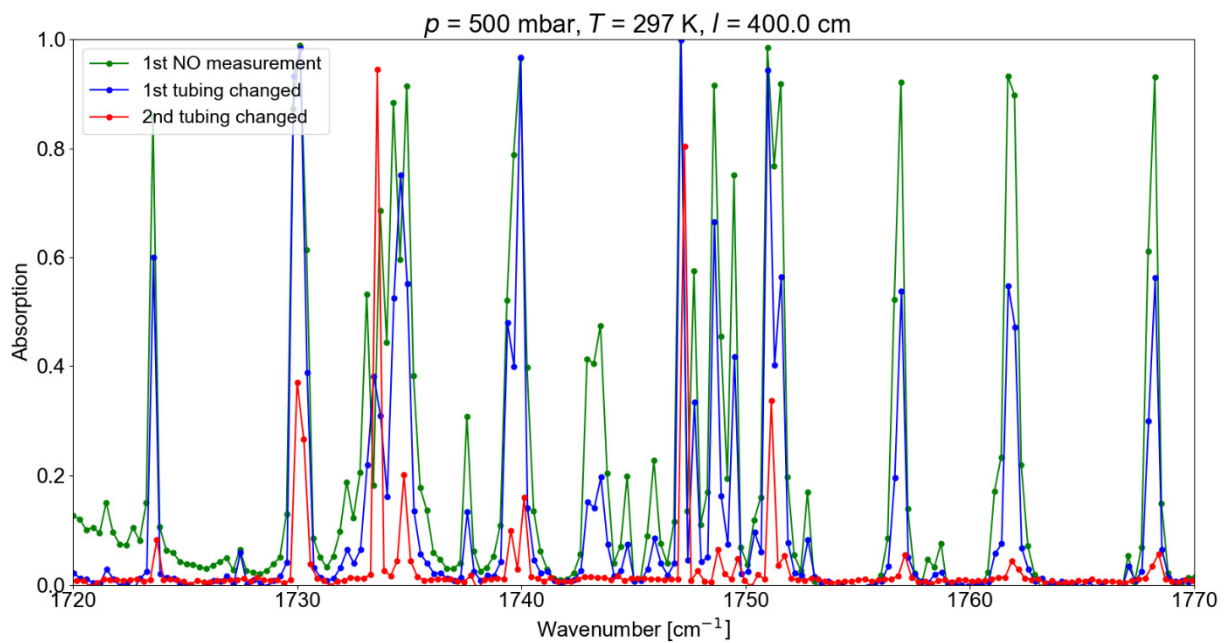
Fig. 23: The change to steel tubings reduces the water content during NO measurements (p = 500 mbar).

- Duration of evacuation

  The vacuum pump was only activated prior to the experiment when the measurements were started. Coincident with the purging start, the cell was evacuated around 30 minutes before the experiments started. It was found that this time is not sufficient to expurgate especially the parasitic water molecules. The absorption features of any measurement were supplemented by features due to water absorption. Looking at the absorption outline after the exchange of tubings in **Fig. 23** (red line), there are still some absorption peak, although there should be zero absorption in an ideal set-up for the used non-absorbing gas Helium.
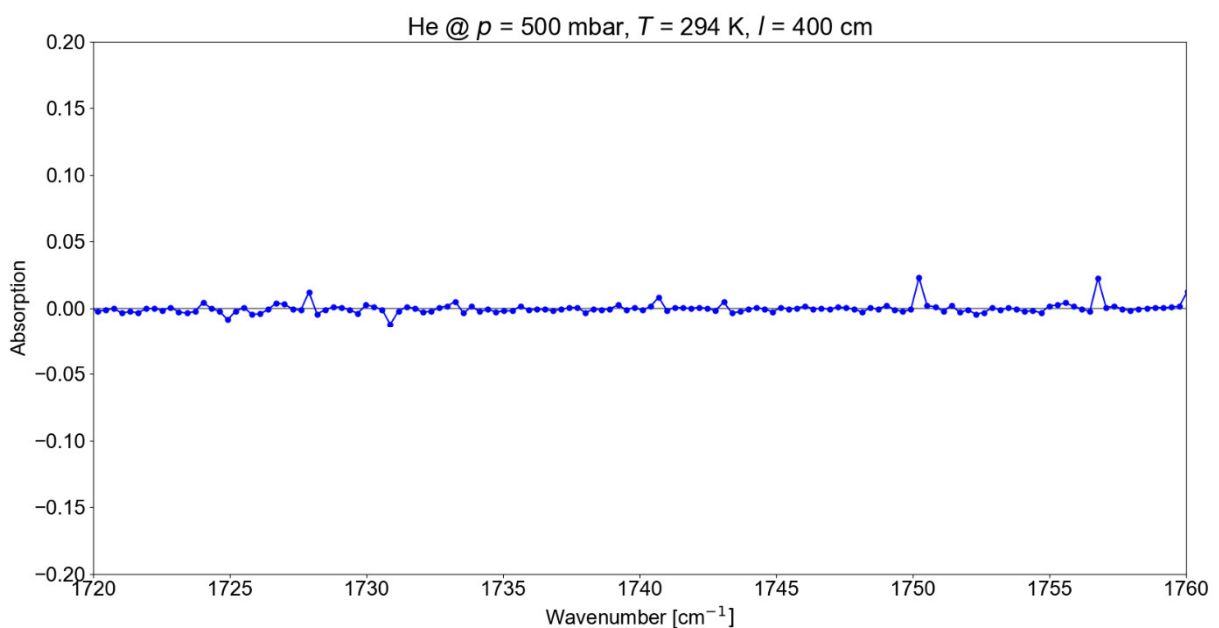
Fig. 24: Extending the evacuation time of the cell, the water content is reduced further.

  To prevent that, the vacuum pump operated continuously from there on, which increased the measurement quality significantly. **Fig. 24** shows that the prolongation of the evacuation time leads to an absorption-reduced spectrum for Helium. There are some deviations visible, which hint to a remaining fraction of water inside the cell. This aspect is discussed in the actual measurement results (section 4.3).

- Normalization issues

  What was evident already in the first *LongTerm* measurements (**Fig. 25**), became latest obvious during the first *StepSweeping* measurements. With increasing pressure,

the normalization did not work out which can be seen by the shift of the baseline in **Fig. 26** and **Fig. 27**. The shift should not appear as where full transmission (100 %) occurs the absorption baseline is expected to be located at 0 for these spectral points and at least there shouldn't be any negative values.
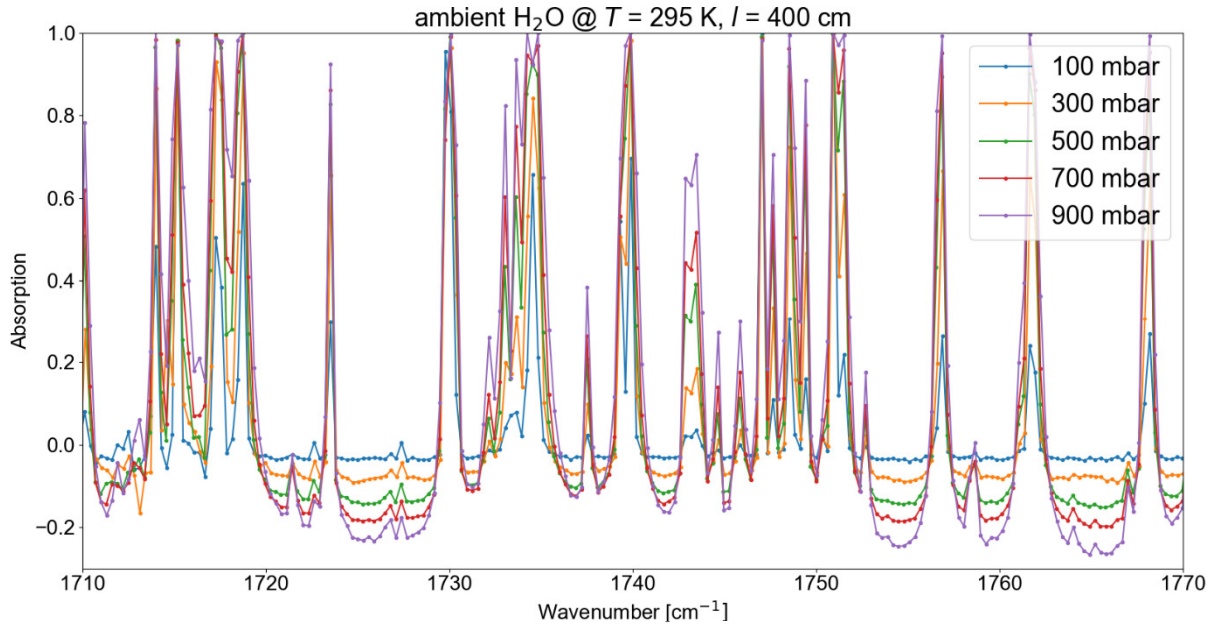
Fig. 25: Inserting gas at various pressures yields normalization issues. Measurement carried out in *LongTerm* mode with ambient H_2O.
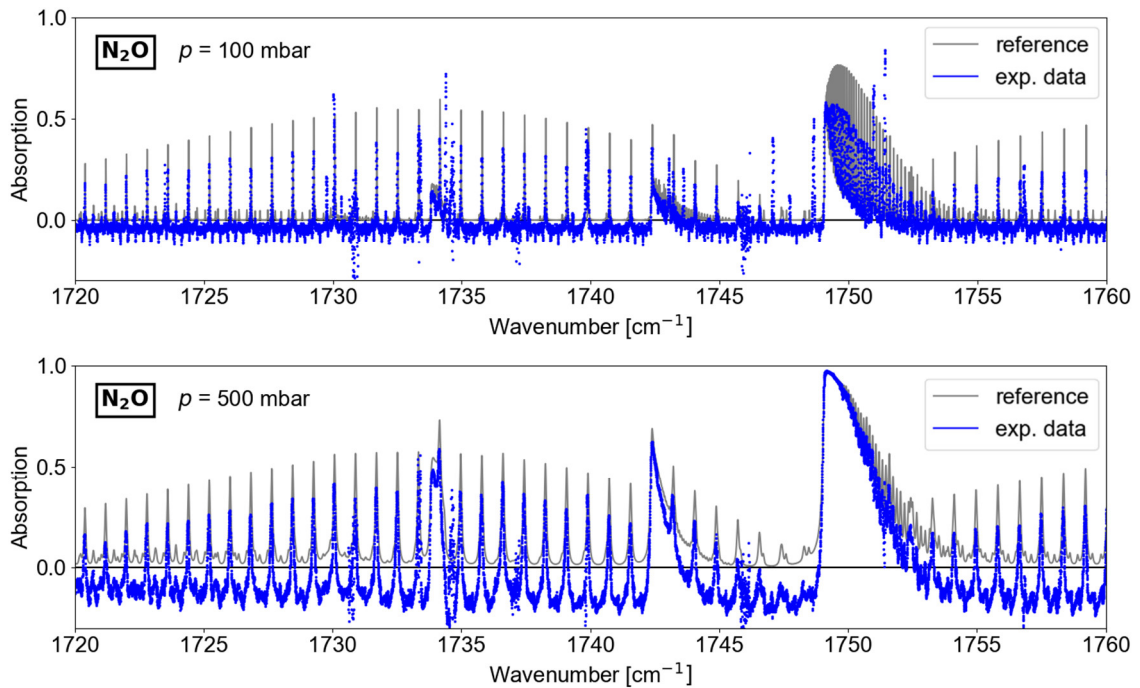
Fig. 26: The baseline offset is larger for higher pressure in a *StepSweeping* N_2O measurement.
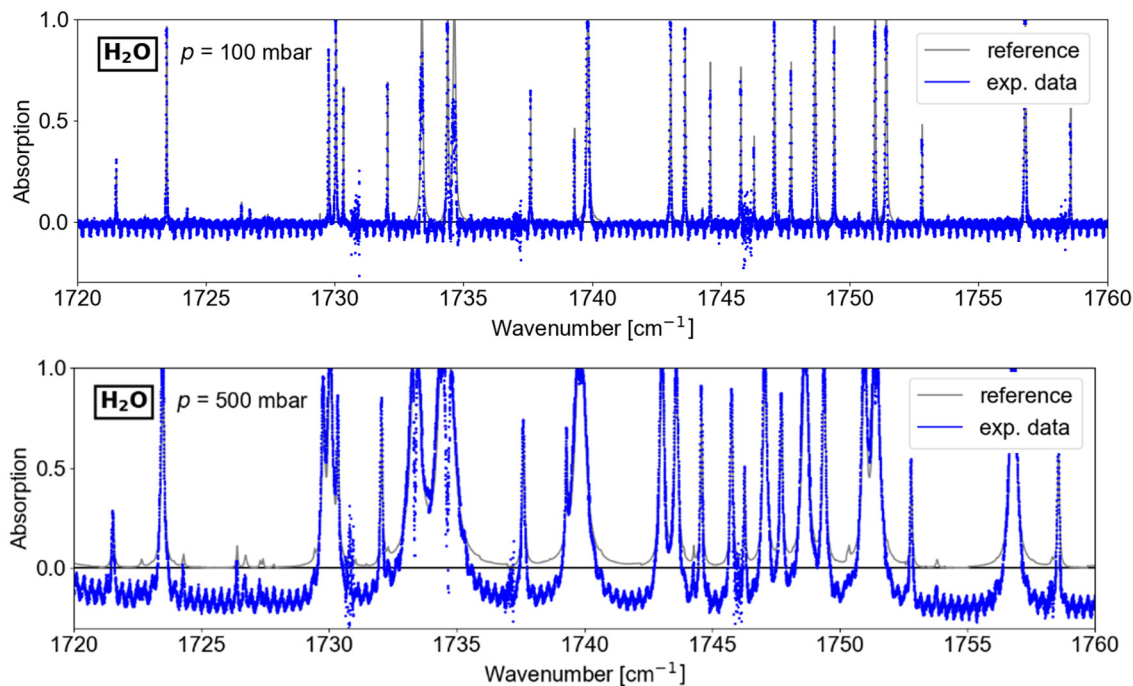
Fig. 27: In *StepSweeping*, H$_2$O measurements (~ 6800 ppm) display a baseline offset as well.
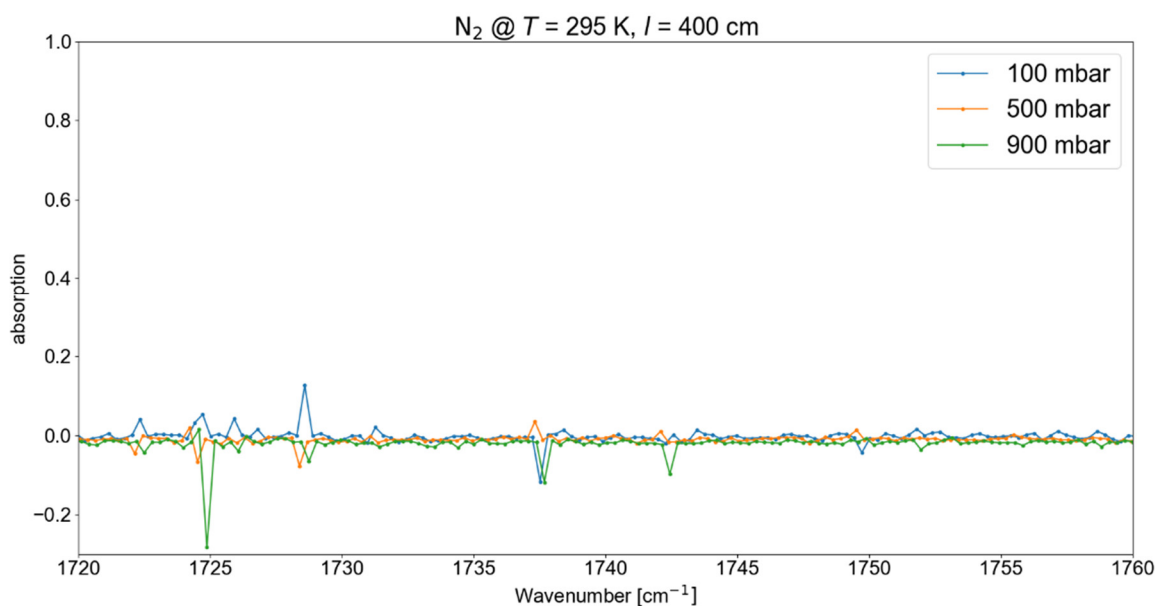
Fig. 28: A baseline shift for N$_2$ at different pressures is visible but not as strong as for the other species. The small deviations originate from remaining water molecules as the cell was not perfectly purged meanwhile.

It is observed that an increased amount of gas (higher pressure) results in a stronger displacement of the baseline. As shown in **Fig. 28**, a minor baseline offset is even

visible for tests with the non-absorbing N_2. The appearance of the baseline shift depends on gas species and pressure. This behavior confirmed that the offset of the baseline is correlated to the strength of absorption lines: the stronger the absorption features for a given species and pressure, the stronger the shift of the baseline. The offset was reproducible for a larger number of repeated tests and thus not only an effect of bad laser condition or the like.

It was then found that this behavior is correlated to the saturation of the detector. In this case, strong absorption leads to a reduction of the sample detector's saturation, and thus higher signal for non-absorbed lines. To overcome that, the total signal power difference needs to be decreased. Therefore, an additional aperture is placed in the beam path right in front of the detector. It was closed in way that only one third of the previous power reaches the detector, as that was found the optimal way to consider this effect.

- Back reflections and optical feedback

As described for the experimental set-up, the external configuration requires a precise coupling system using a fiber polished at Brewster angle to allow maximum signal input. Although the in-coupling at Brewster angle promises full transmission, it was observed that back reflections cause optical feedback. The fallback rate was highly fluctuating indicating some problem with the heterodyne signal. More importantly, the heterodyne signal measured at the detector changed its shape in every acquisition and did not sustain one single shape for a longer while, making it impossible to conduct usable sweeping measurements as a reconstruction isn't possible for a varying heterodyne signal shape during the procedure. Not only the sample but as well the reference beam showed this behavior, indicating that optical feedback might be the source for that. The assumption was confirmed by the fact that the reference beam kept its shape once the sample beam was blocked by any diffuse material (like paper). In conclusion, back reflections from the facets of the fiber leads to optical feedback. To overcome the problem, the fiber was slightly moved away from the direct focal point. Although that came along with a slightly reduced power input to the fiber, it was a necessary trade-off for a stable heterodyne signal.

- Fringing

  Assuming that fixing the fluctuating fallback rate solved the issues around the external set-up successfully, the first tests were carried out with the external Herriott cell in the *StepSweeping* measurement mode. But all the obtained absorption spectra featured a periodic zigzag pattern. In **Fig. 29** (H_2O, $p = 500$ mbar), the pattern is most prominent in regions with no expected absorption such as between $\upsilon = 1725$ cm^{-1} and 1730 cm^{-1}. It is traced with a red line for better visibility. The pattern becomes most obviously visible in a measurement at $p = 0$ mbar as shown in **Fig. 30**. The other outliers present in the spectrum correspond to water absorption, as the spectrometer was not purged appropriately during this experiment, so water absorption influences the beam. The spikes have a periodicity of around 2.5 cm^{-1} and were reproducible for several repetitions under same conditions. If this effect occurred due to bad laser conditions, the periodicity would be expected to be around 0.3 cm^{-1}.
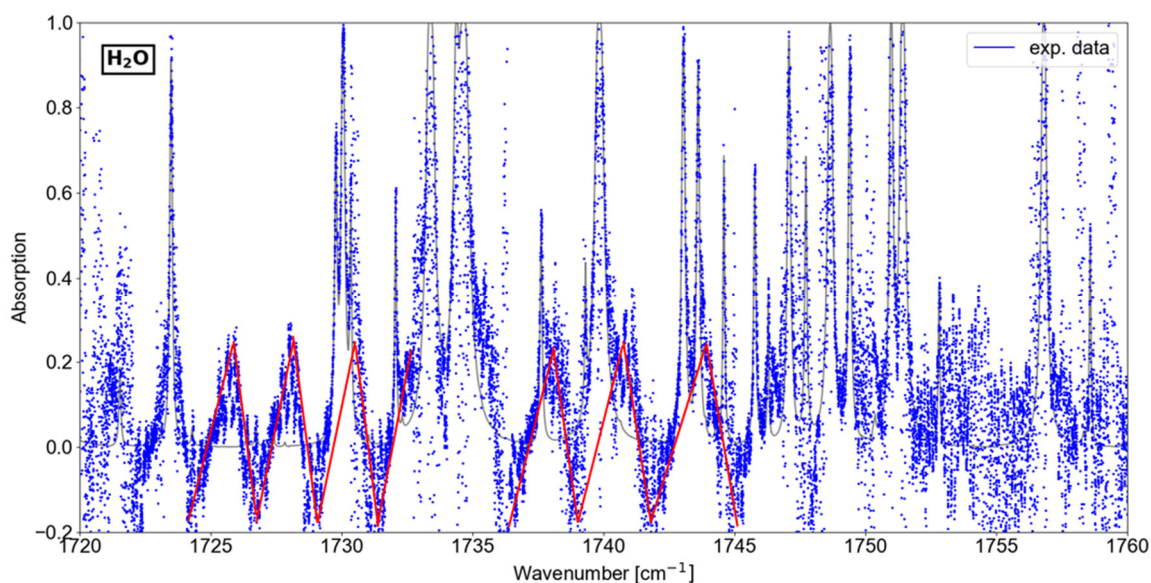
Fig. 29: Red lines highlight the arising zigzag pattern in a H_2O measurement (~4600 ppm, $p = 500$mbar).
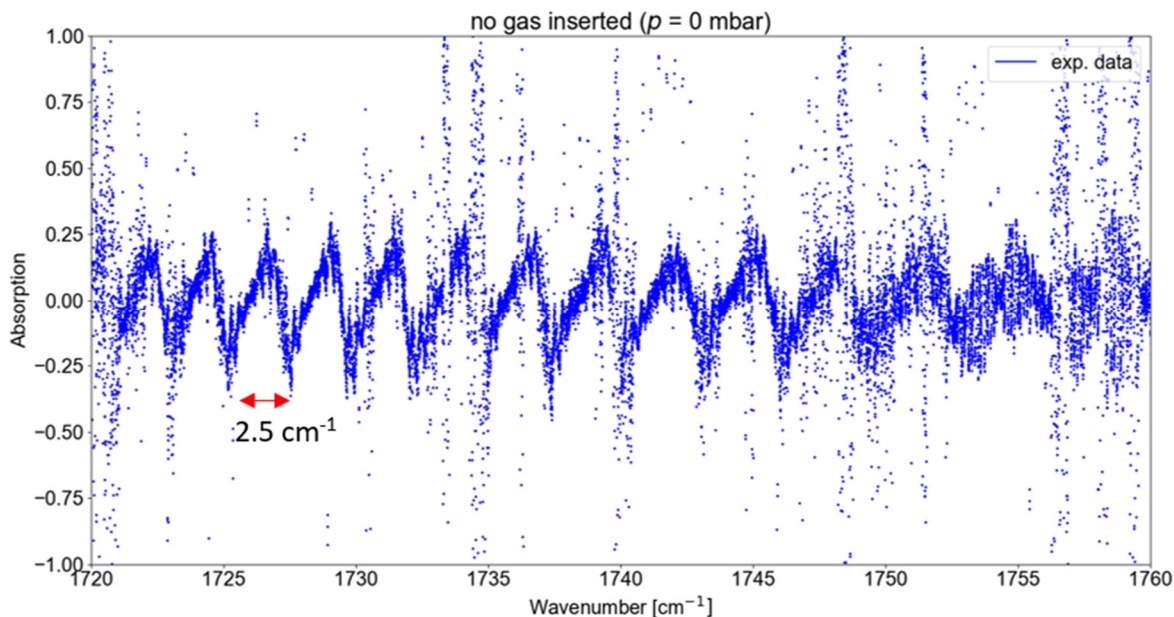
Fig. 30: Periodic zigzag pattern for an experiment without absorption ($p = 0$ mbar) due to fringe effects. Other outlier features correspond to water as the spectrometer was not purged appropriately during this experiment.

In order to actually be able to exclude bad laser conditions as the source, the transmission data of a few individual comb lines were plotted versus the step number. In a measurement without gas insertion, meaning no expected absorption, the transmission should be ideally constant at 1 (= 100%) for each comb line or in reality at least close to 1 without larger deviations, which was the case for earlier measurements in the internal set-up (**Fig. 31** top). Compared to that, the comb lines display a varying deviation from the baseline (**Fig. 31** bottom). It is possible to identify "sets" of comb lines that are correlated and show a similar variation trend with ongoing sweeping step number which is indicated with different color ranges in the **Fig. 31**. Each set consists of some comb lines where roughly every eighth or ninth line is allocated to a set. Since two comb lines, i.e. two initial spectral measurement points, are distanced by $\Delta\upsilon = 0.3$ cm⁻¹, that explains the 2.5 cm⁻¹ periodicity of the zigzag pattern. As the laser conditions don't cause the zigzag pattern, the distortions are associated with so-called fringing. Fringes usually result from reflections inside the sample or from reflections among the optical components in the beam path. These reflections lead to additional interferences. By that, fringes change the relative peak heights, thus their appearance hinders the reliable interpretation of data on the

digitizer. There are post-processing approaches for the removal of fringes by fitting sinusoidal functions to them, albeit it is preferable to prevent the arising of the fringing effect at all. In this work, it was attempted to minimize the fringe noise by further adjusting the beam path, which was not optimally achieved, but results are presented later regardless.
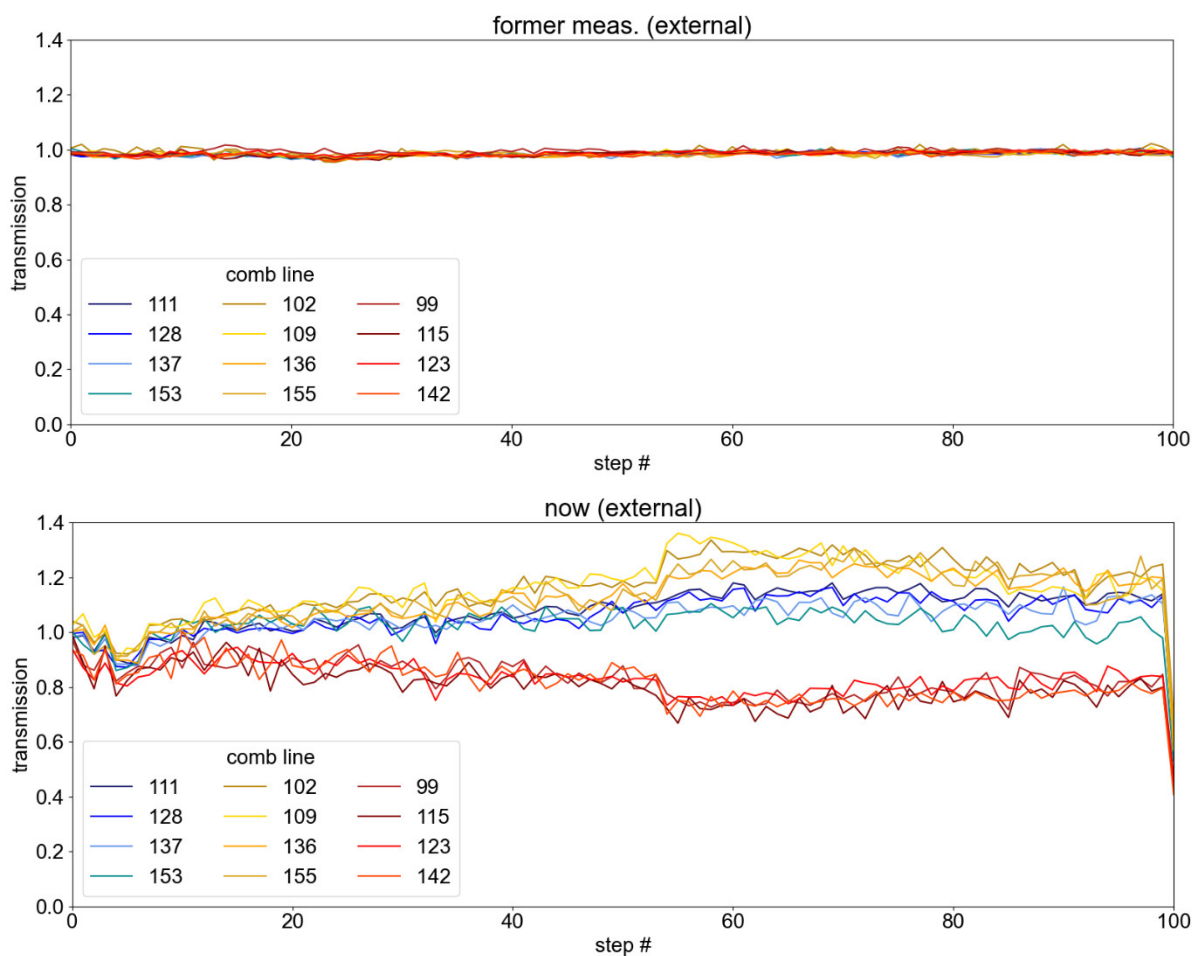
Fig. 31: Transmission data for individual comb lines indicate that the fringing effect occurs in the external set-up. Similar colors indicate correspond to sets of comb lines that show a similar variation pattern.

4.3. Internal Herriott Cell

LongTerm measurements
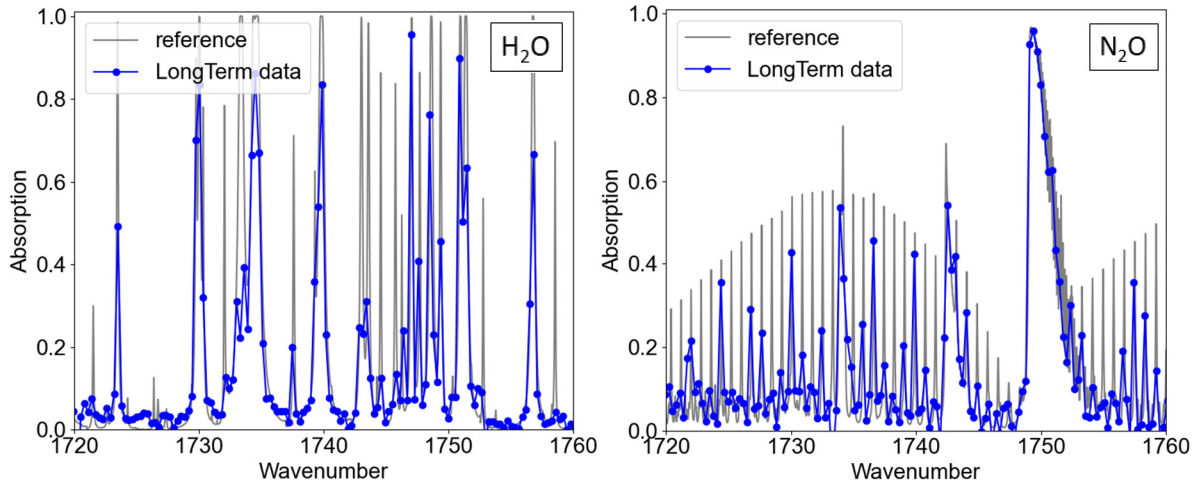
Fig. 32: *LongTerm* measurements for H_2O (left) and N_2O (right) at $p = 500$ mbar, $T = 295$ K.

First, measurements in the standard *LongTerm* mode were performed. As shown in **Fig. 32** for H_2O and N_2O ($p = 500$ mbar, $T = 295$ K), the data at the measured spectral positions align well with the simulated HITRAN reference spectrum. But it has to be noted that not all absorption features are fully resolved. As inferred from a zoom on specific features (**Fig. 33**), it is obvious that the spectral distance is too large between adjacent spectral points.
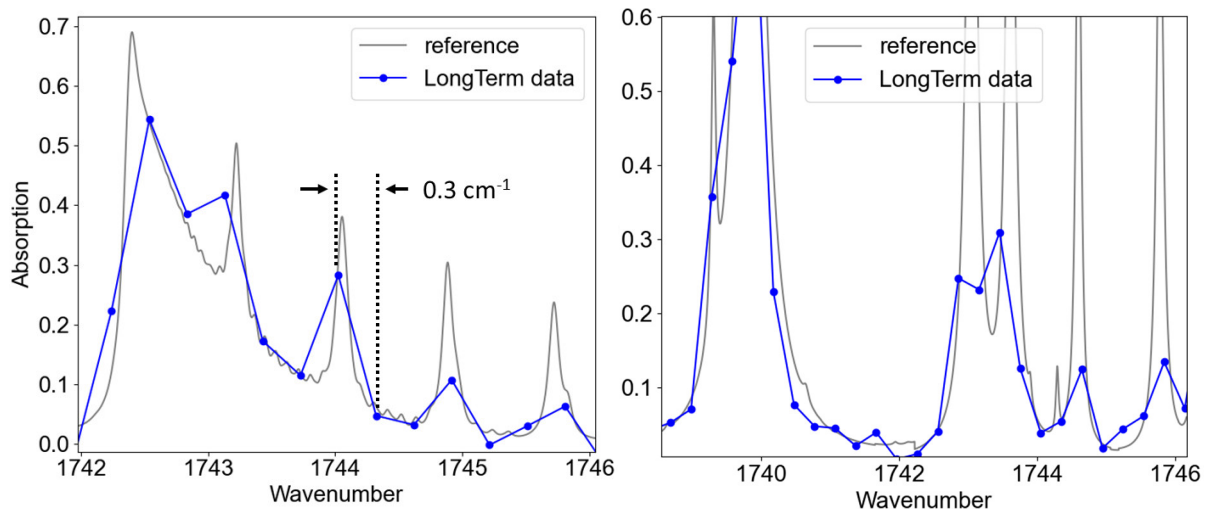
Fig. 33: The large spectral point distance results in unresolved absorption features.

StepSweeping measurements

The *StepSweeping* overcomes the issue of a too large point spacing by modulating current and temperature as described in section 3.2. Each acquisition at specific current and temperature conditions is averaged over a defined number of samples. A higher number of samples N increases the signal-to-noise ratio (SNR). But is has to be noted that the sample number correlates to the acquisition length. When the spectrometer takes acquisitions with a rate of $2 \cdot 10^9$ samples/s, the acquisition length t_{aq} scales with N as:

$$t_{aq} = N/(2 \cdot 10^9) \text{ s.}$$

Although a higher SNR is desirable, a large acquisition length isn't compatible with the necessary speed for the tuning process. To make the following measurements with varied stabilization times comparable, the number of samples per acquisition is set to $N = 2\textasciicircum 17$ as this sets the acquisition length shorter.

Although the cell is evacuated long-time and the sample compartment purged prior to measurements, single water molecules are remaining in the measurement area. Measurements at $p = 0$ mbar reveal the relevant wavenumber regions. As shown in **Fig. 34**, the parasitic molecules influence both background and sample measurement and thus result in outliers that are positive or negative, which makes no sense from a physical point of view. These regions, marked with red in the figure, are identified and afterwards masked out in the evaluation of other measurements. An example for the masking process is presented in **Fig. 35**, where masked points are colored red.
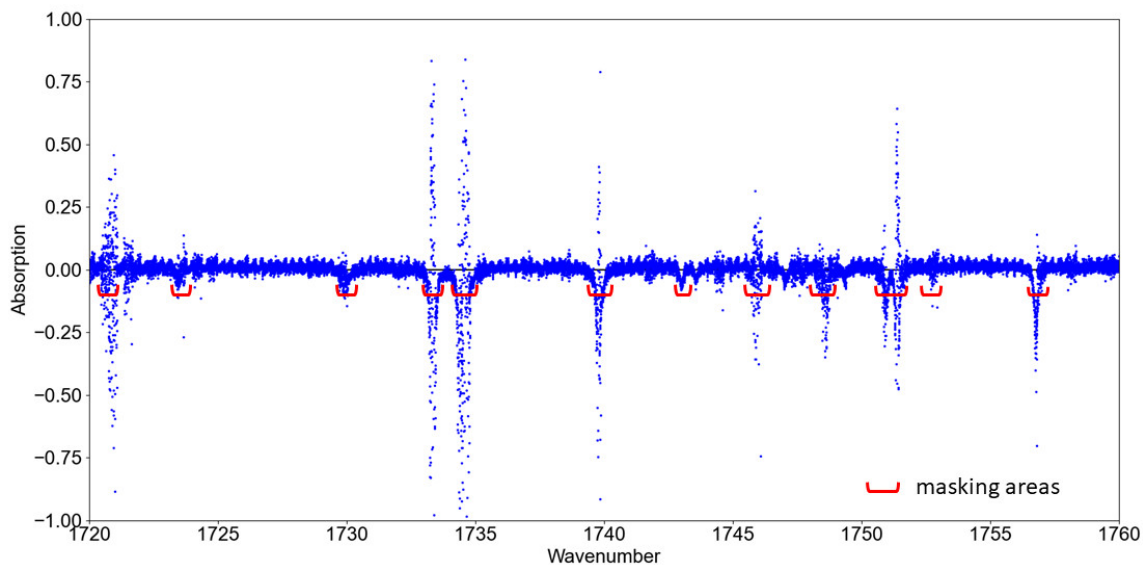
Fig. 34: Measurement at p = 0 mbar reveals outliers originating from remaining water molecules.
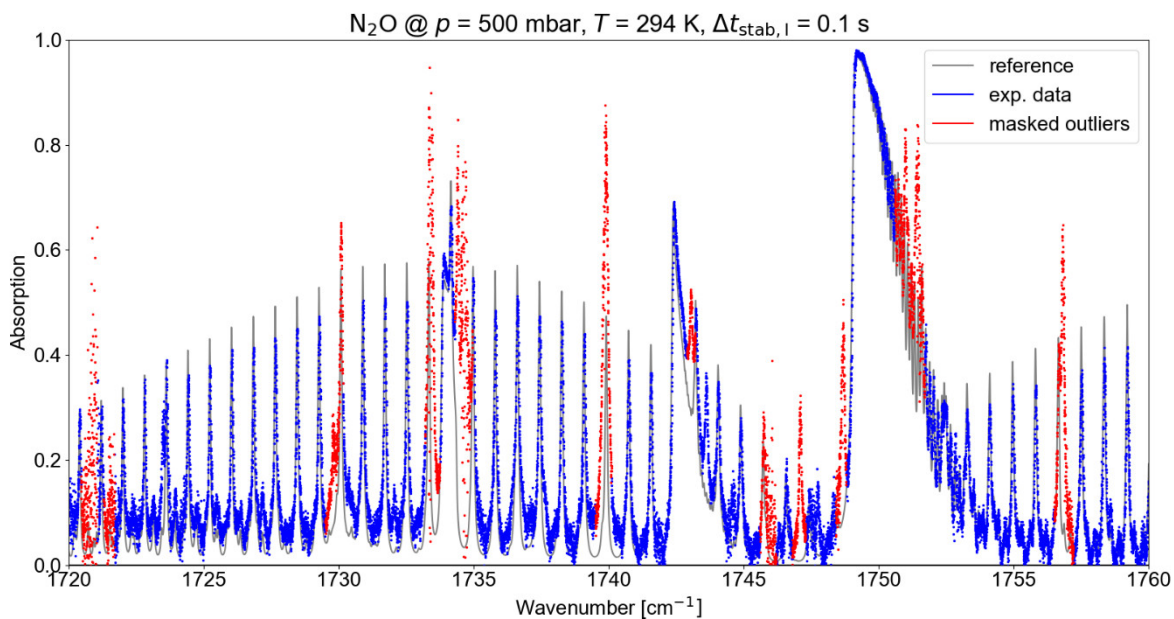
Fig. 35: Red colored markers indicated the parasitic areas that are masked out for the analysis.

Fig. 36 and **Fig. 37** show the results from the *StepSweeping* measurements with N_2O and H_2O at different pressures, respectively. Now obviously all absorption features are resolved compared to the previous *LongTerm* measurements. This is confirmed by a detailed view in **Fig. 38**. As expected, the *StepSweeping* procedure closes the gap between adjacent points, thus resulting in an improved depiction of the features.

Regardless of the attempt to consider the normalization (section 4.2), it has to be noted that for higher pressures the baseline is still slightly shifted and the non and weakly absorbed areas don't match with the reference amplitudes. Red circles highlight this exemplarily in **Fig. 36**. For lower pressures, the regions with low absorption match with the reference but the amplitudes of the peaks are lower than in the reference simulation. The opposite behavior is apparent at higher pressures where the heights of the peak amplitudes suit well to the reference but there are clear deviations from lower absorption regimes. This effect is stronger evident for N_2O than in the H_2O spectra which may be inferred to the greater number of absorption features for N_2O.

Another interesting observation is the fact that the deviations differ depending on the wavenumber region. Looking at the N_2O spectrum at $p = 900$ mbar, the deviations are larger at lower wavenumbers (left side in plot) compared to those at higher wavenumbers. A reasonable explanation for that cannot be given but this should be investigated further as it seems to be a systematic error.

Besides that, it has to be noted that while the peaks themselves are resolved appropriately in their width and location, there are relatively large deviations of up to 5% around the baseline or at regions with less of absorption. It was naively thought that this is a normal noise in *StepSweeping* mode as a trade-off. But although there is no obvious zigzag pattern as earlier shown in **Fig. 30**, fringing is a reasonable explanation for this case as well. As at the beginning the beam path was aligned well (see section 4.2), there must have been an unintended minimal change in the beam path during the measurement performance, resulting in small fringes. Unfortunately, we learned about the possibility of fringing just later in the process for the external set-up where it was obvious, therefore there was no attempt of re-optimization of the beam path to prevent this effect.
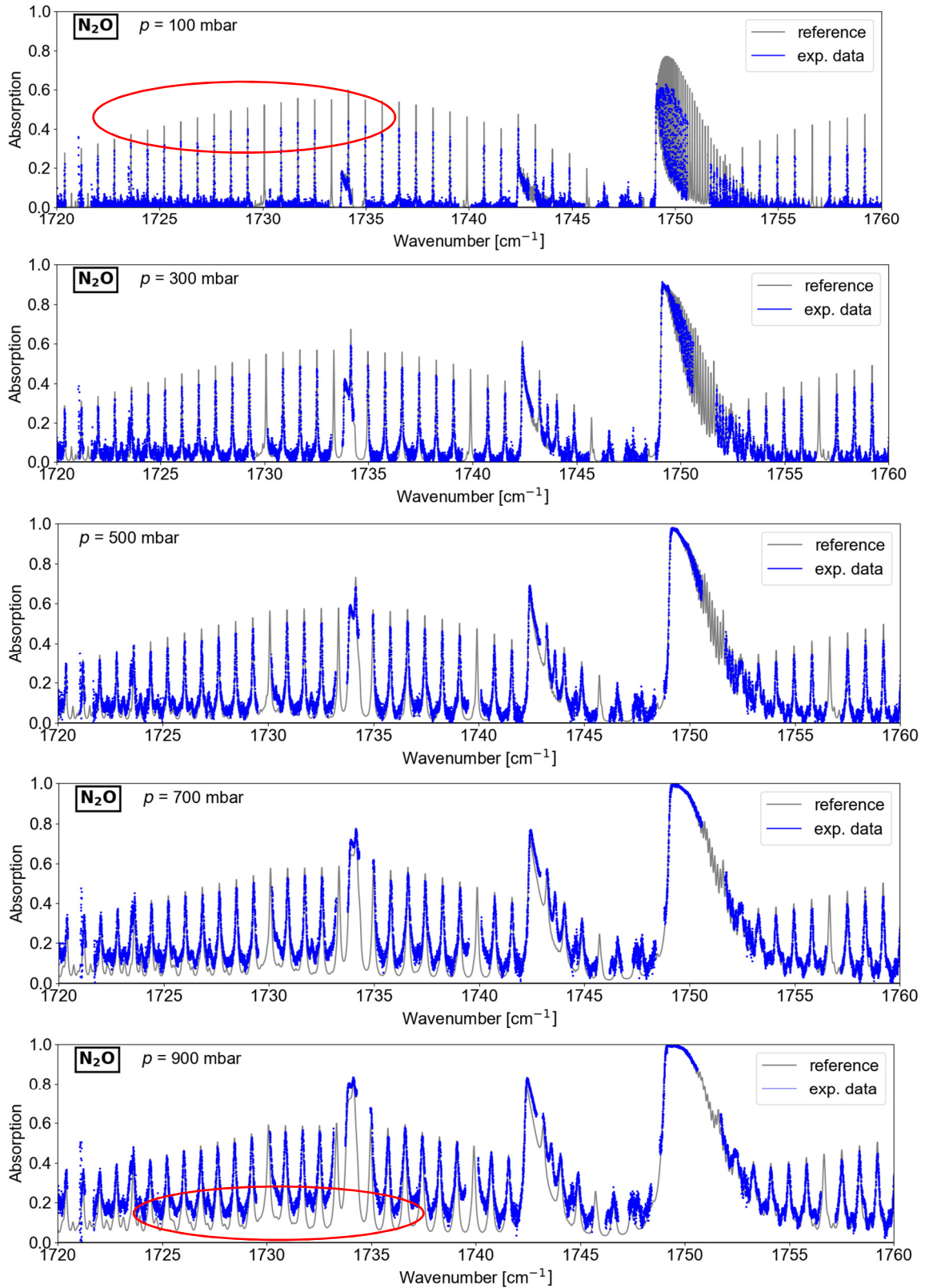
Fig. 36: N₂O measurement at different pressures in *StepSweeping* mode. The red circles highlight example regions with large deviations from the reference.
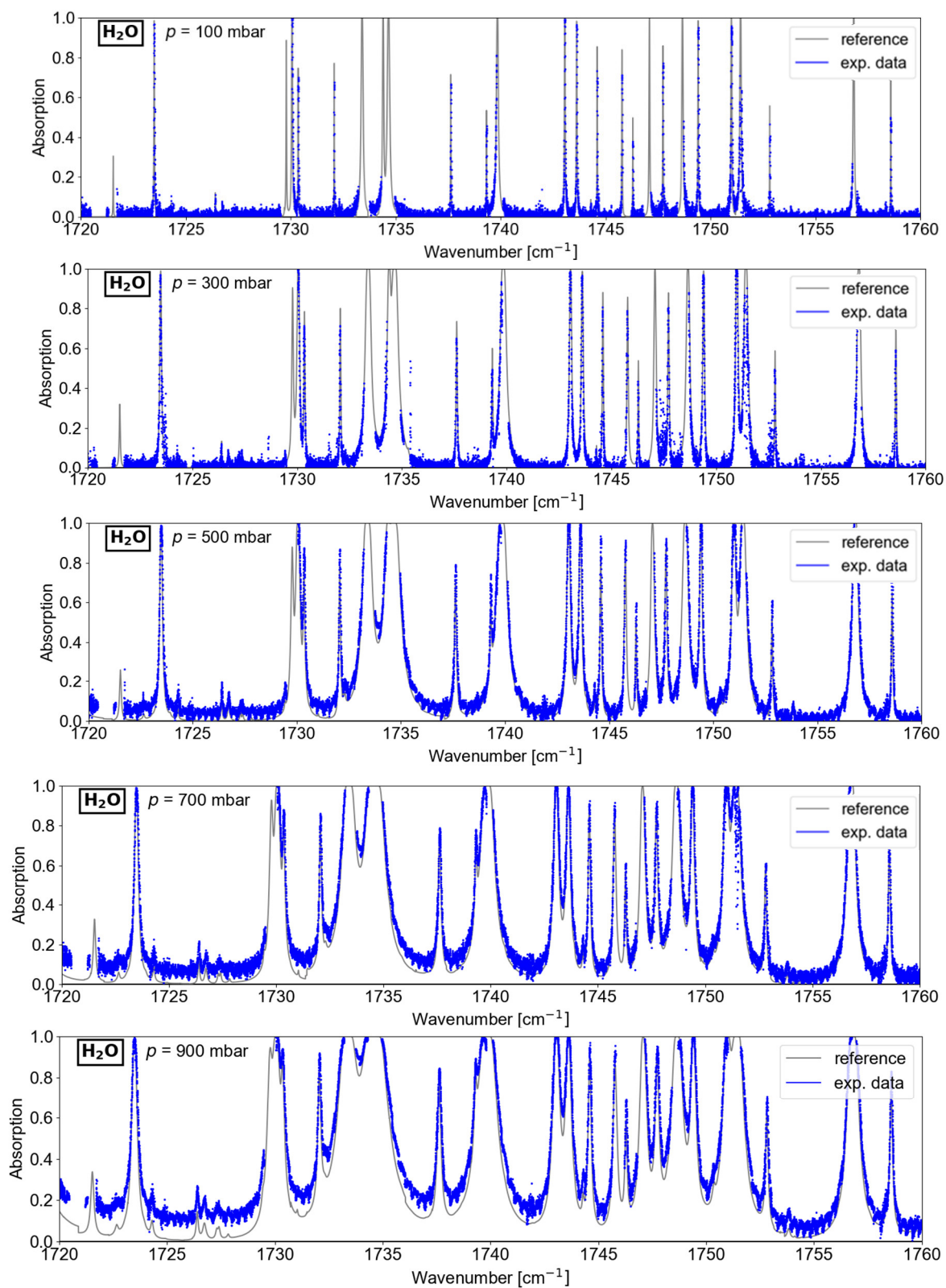
Fig. 37: H₂O measurement at different pressures in *StepSweeping* mode.
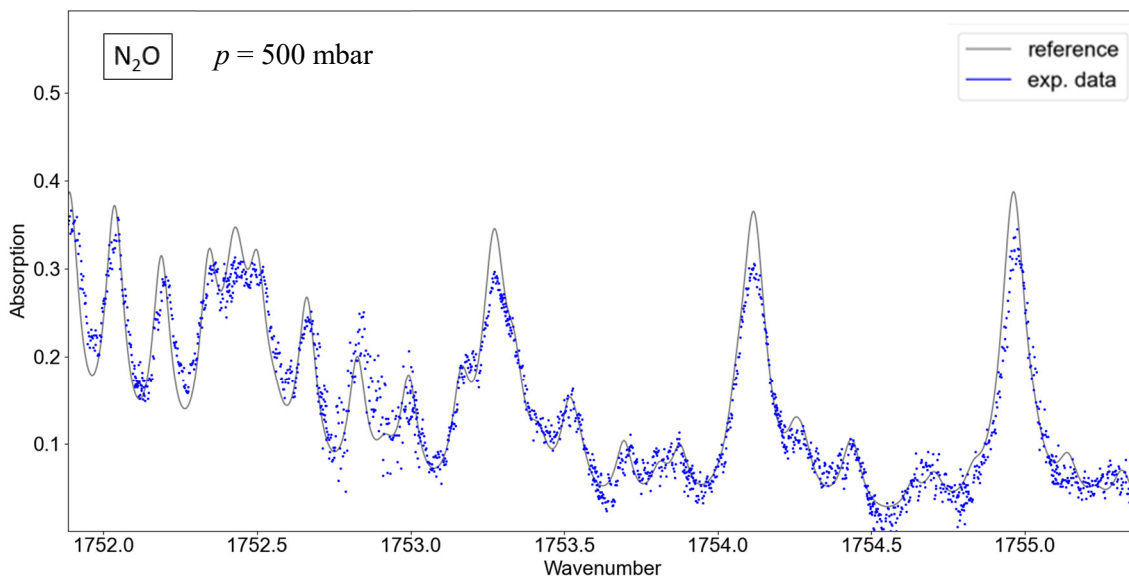
Fig. 38: Zoomed view on N₂O measurement (p = 500 mbar, T = 294 K) in *StepSweeping* mode. All absorption features are resolved due to the reduction of spectral point spacing.

A single measurement for NO (5000 ppm) was performed. **Fig. 39** presents the obtained absorption spectrum. As confirmed with the red line for HITRAN reference, NO can be adequately measured despite its rather weak absorption. Beside the NO absorption lines, there are absorption features clearly corresponding to H_2O. Based on the strength of the absorption lines and the pressure and temperature parameters, the water content is estimated to be around 450 ppm as indicated with the yellow line in **Fig. 39**. Although that was unplanned, it confirms that multi-species measurements and consequent reconstruction of gas species concentration are actually possible. It has to be noted that the measurement accuracy suffers from larger variations around the baseline with deviations of up to $\pm$ 5% from the baseline. This is ascribed to fringing effects as well, so the beam path was not optimal during the test.
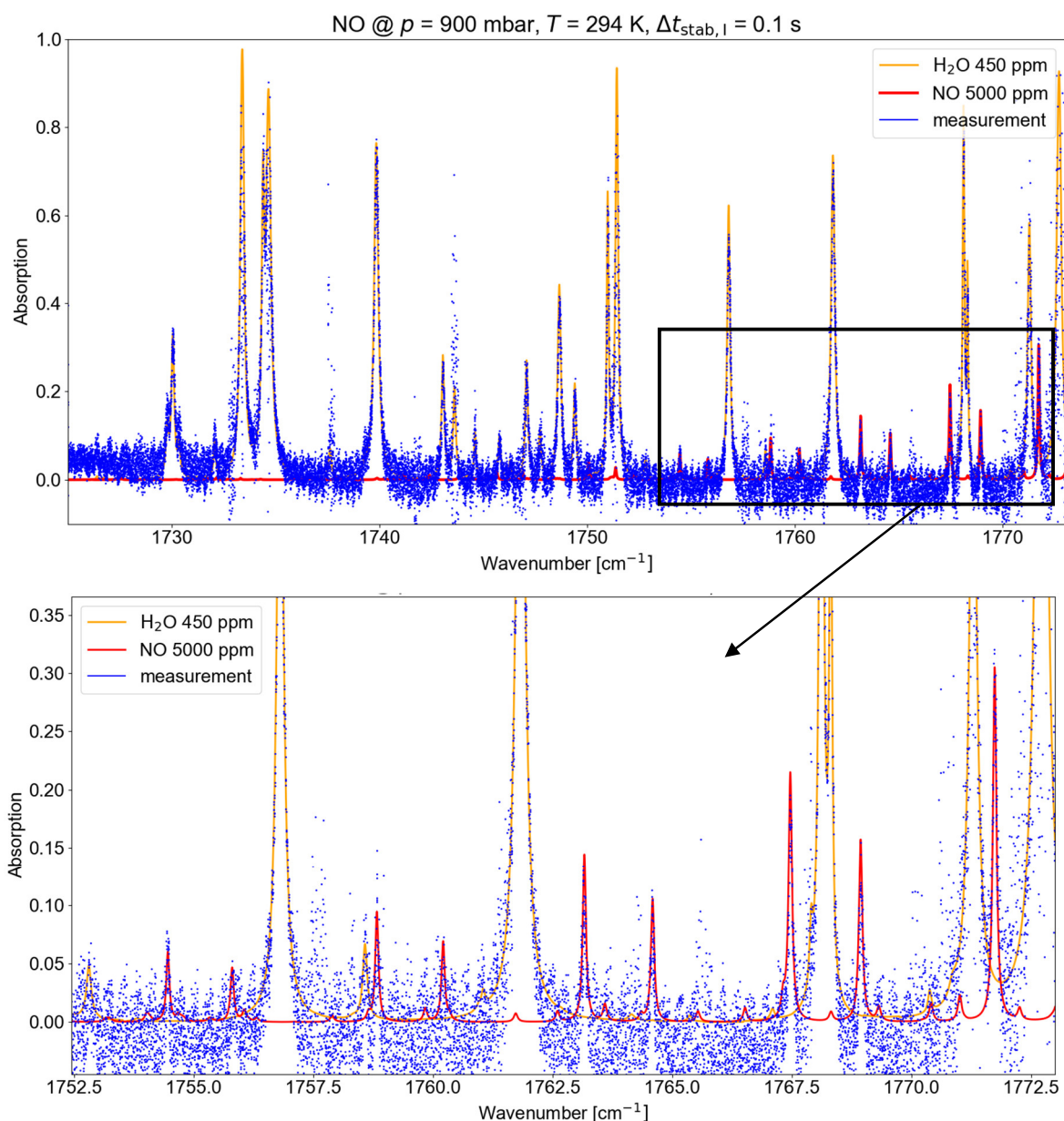
Fig. 39: The NO measurement includes clear water features. By using them, the water content can be estimated to around 450 ppm. Top: full measurement range. Bottom: zoomed view to NO absorption features.

Variation of stabilization time

By eye, the spectra obtained with different stabilization times seem quite similar, as shown in **Fig. 40** and **Fig. 41**.
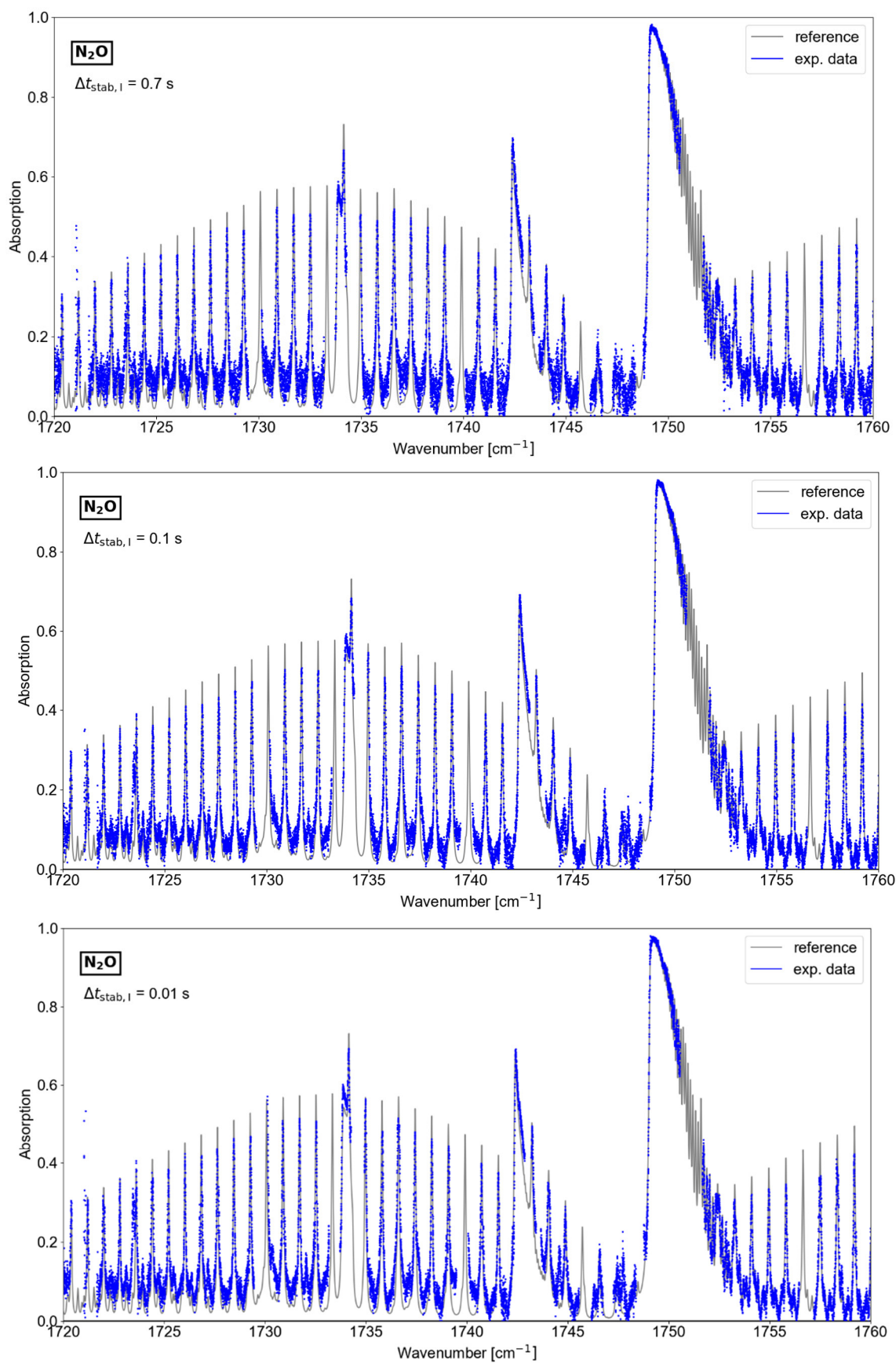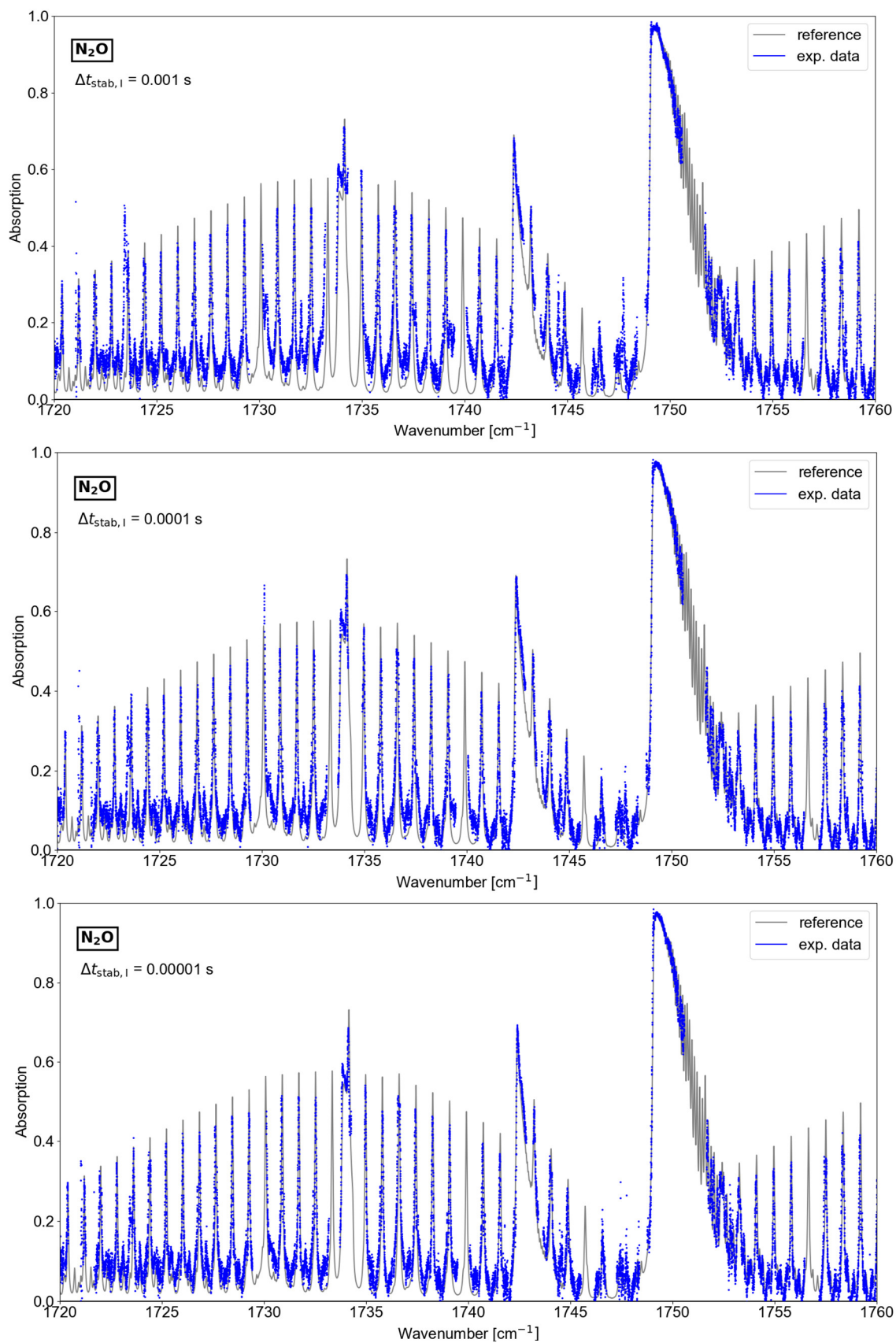
Fig. 40: N₂O measurements with different stabilization times (p = 500 mbar, T = 294 K).
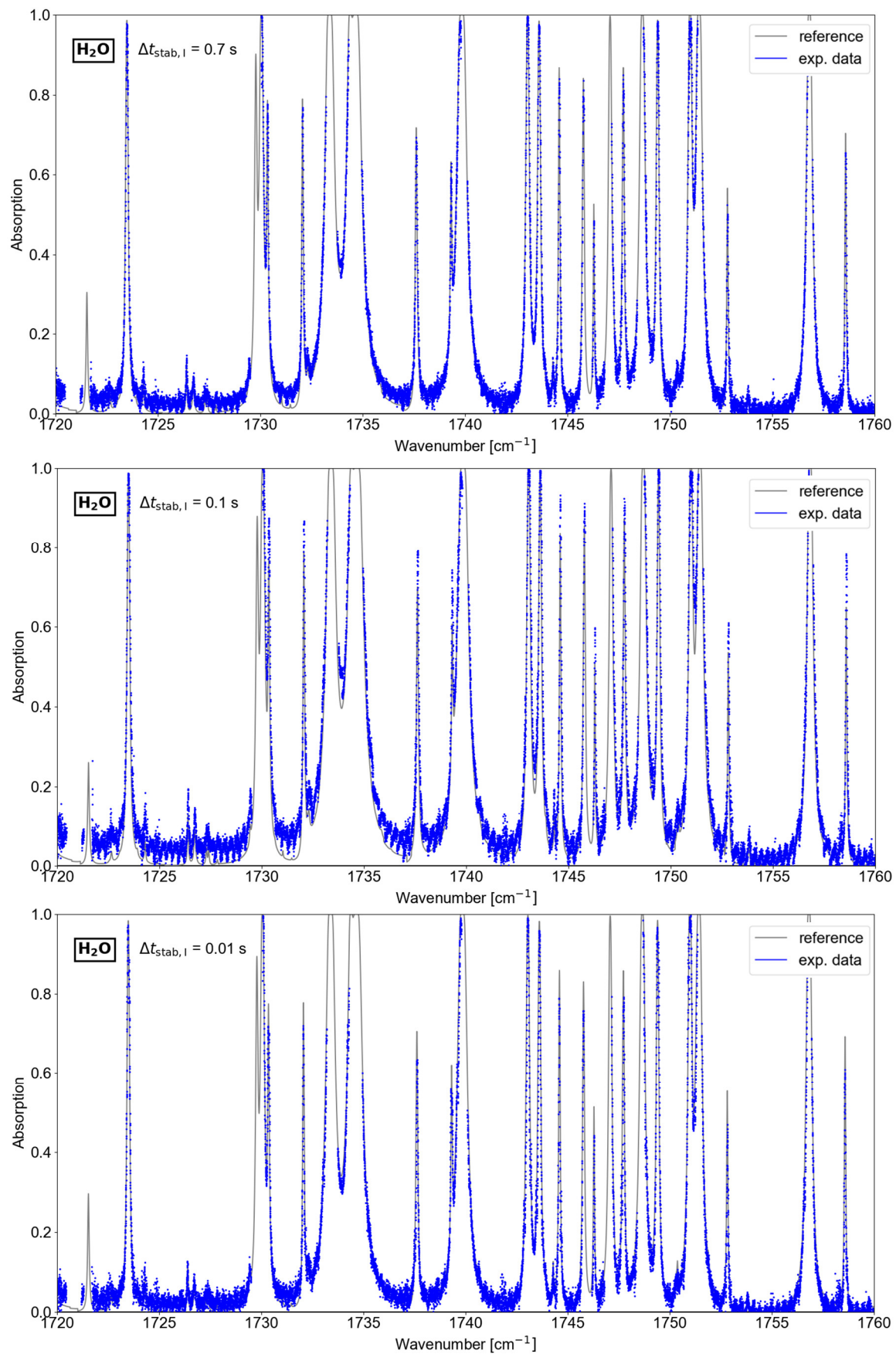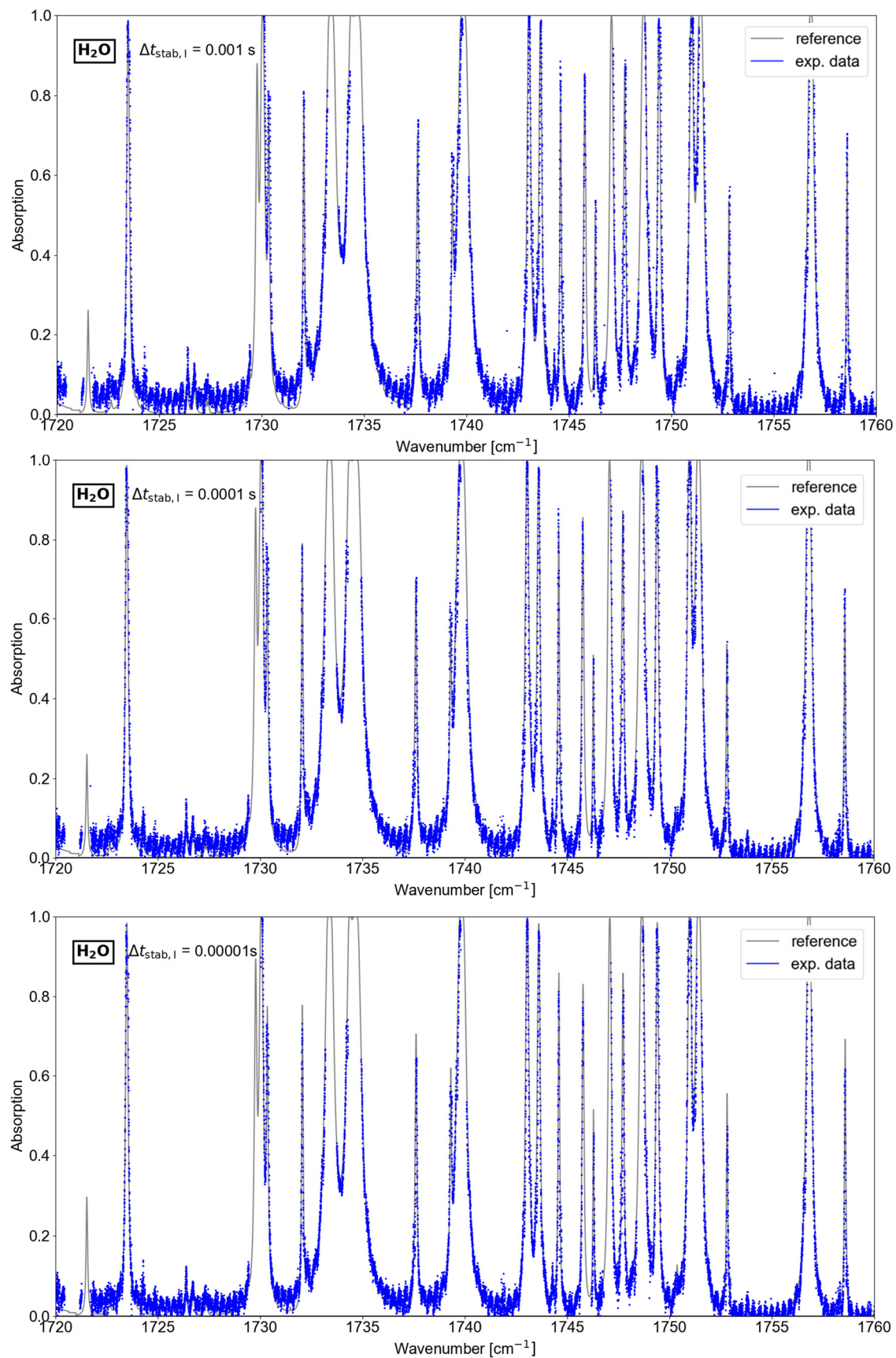
Fig. 41: H$_2$O measurements with different stabilization times (p = 500 mbar, T = 294 K).

For a quantitative comparison for the impact of the current stabilization time, the root mean square (RMS) for deviations of experimentally measured amplitudes y_{exp} from the reference amplitudes y_{ref} for all M spectral measurement points is calculated according to:

$$y_{\text{RMS}} = \sqrt{\frac{\sum_{n=1}^{M}\left(y_{\text{exp},n} - y_{\text{ref},n}\right)^2}{M}} \tag{4.1}$$

Here, the RMS is averaged over three repeated measurement series. As presented in **Fig. 42**, the RMS deviation tends to rise slightly for shorter current stabilization times. But considering that the current stabilization time is reduced over almost five orders of magnitude between $\Delta t_{\text{stab,I}} = 1$ s and $\Delta t_{\text{stab,I}} = 0.00001$ s, the deviation seems negligible. Therefore, it is promising for minor loss in quality when switching to the *FastSweeping*.
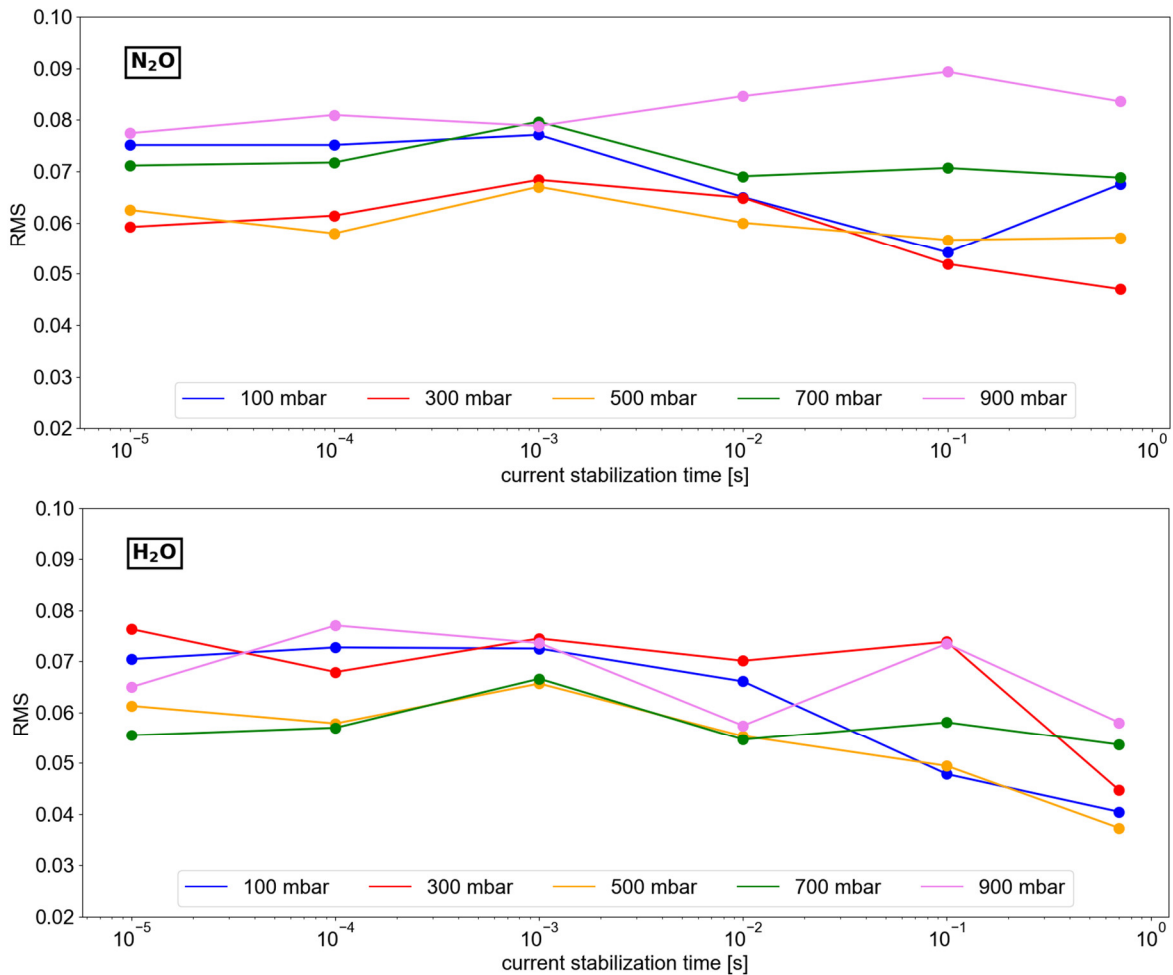
Fig. 42: RMS calculation for H_2O and N_2O measurement versus the current stabilization time step. Colors indicate different pressures.

4.4. External Herriott Cell

The used optical fibers reduce the transmitted power significantly when the Herriott cell is placed externally. Although using a filter with 50 % transmission instead of only 10 % as before, the sample detectors receives only roughly a quarter of the power difference between blocked (no light) and open shutters compared to the one in the internal set-up without optical fibers. This can be explained by the back reflections occurring from in- and outcoupling of the fibers which reduce the power strongly.

A precise alignment of the beam path is for this application thus mandatory. As described earlier, a perfect beam path was unfortunately not achieved, so the results still suffer from the fringing effect. Regardless, the results are presented in the following. **Fig. 44** and **Fig. 45** show the exemplarily spectra resulting from the performed H_2O and N_2O measurements, including more noise. The spectra for N_2O don't differ significantly compared to the internal set-up. The spectra for H_2O differ from the previous ones which is deduced to a lower relative humidity, leading to less water contained in the ambient air and thus weaker absorption features. The reference for the calculated water content (~ 3830 ppm) agrees with the data.

It has to be noted that water absorption is an issue during this specific application, as shown in **Fig. 43**. Besides the parasitic water molecules remaining in the cell despite evacuation, the stronger water influence originates from the open beam path between the coupling units and the Herriott cell. The area is not fully shield from ambient air, so the beam travels around 4 cm through the air where water molecules absorb parts from it.
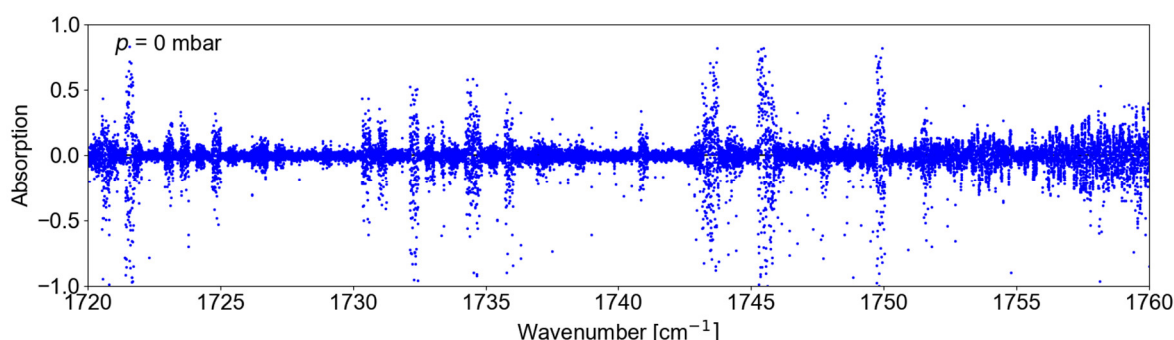
Fig. 43: The revealed outliers originating from ambient water absorption due to open path in external set-up.
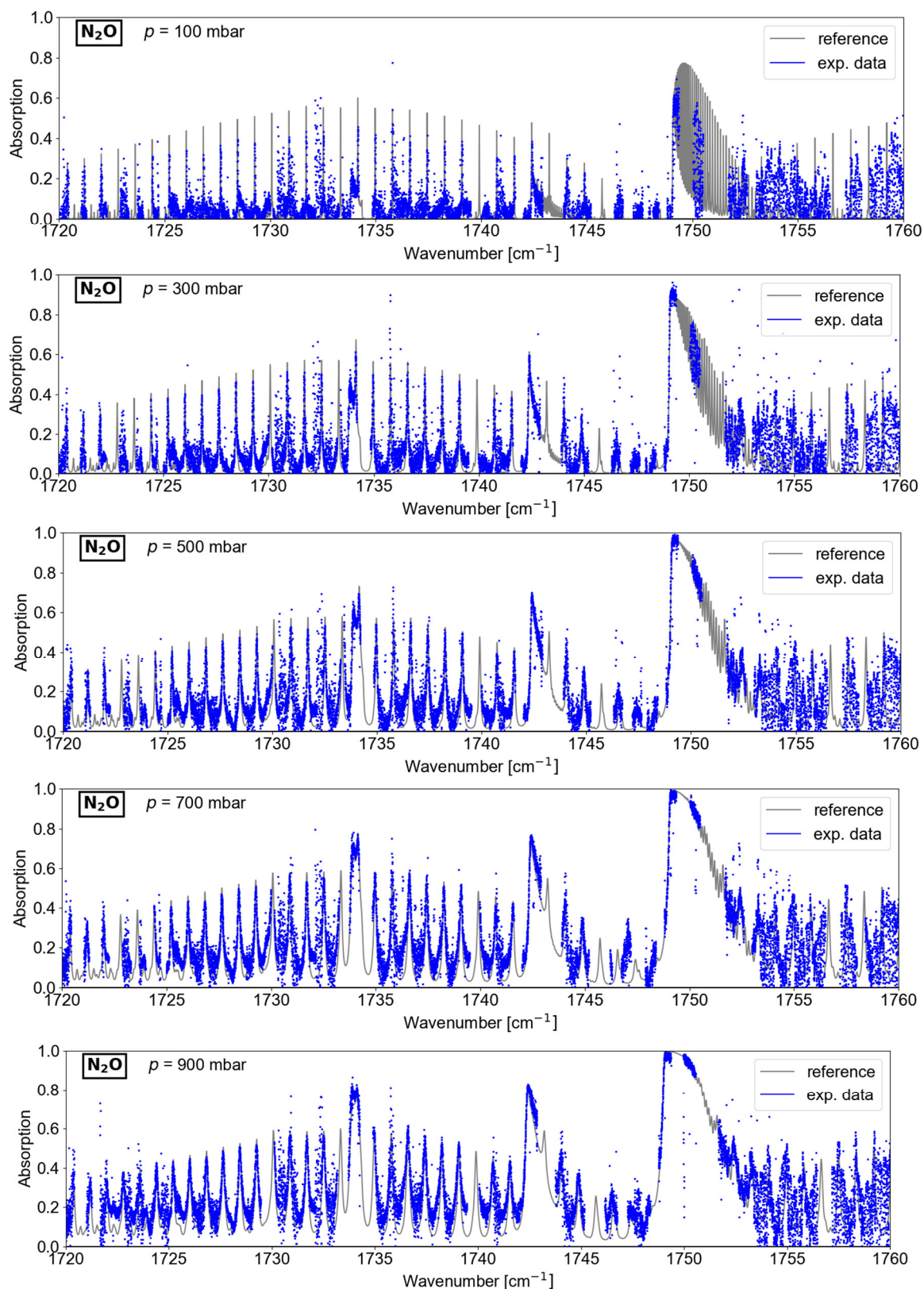
Fig. 44: N₂O measurements at different pressures in external set-up.
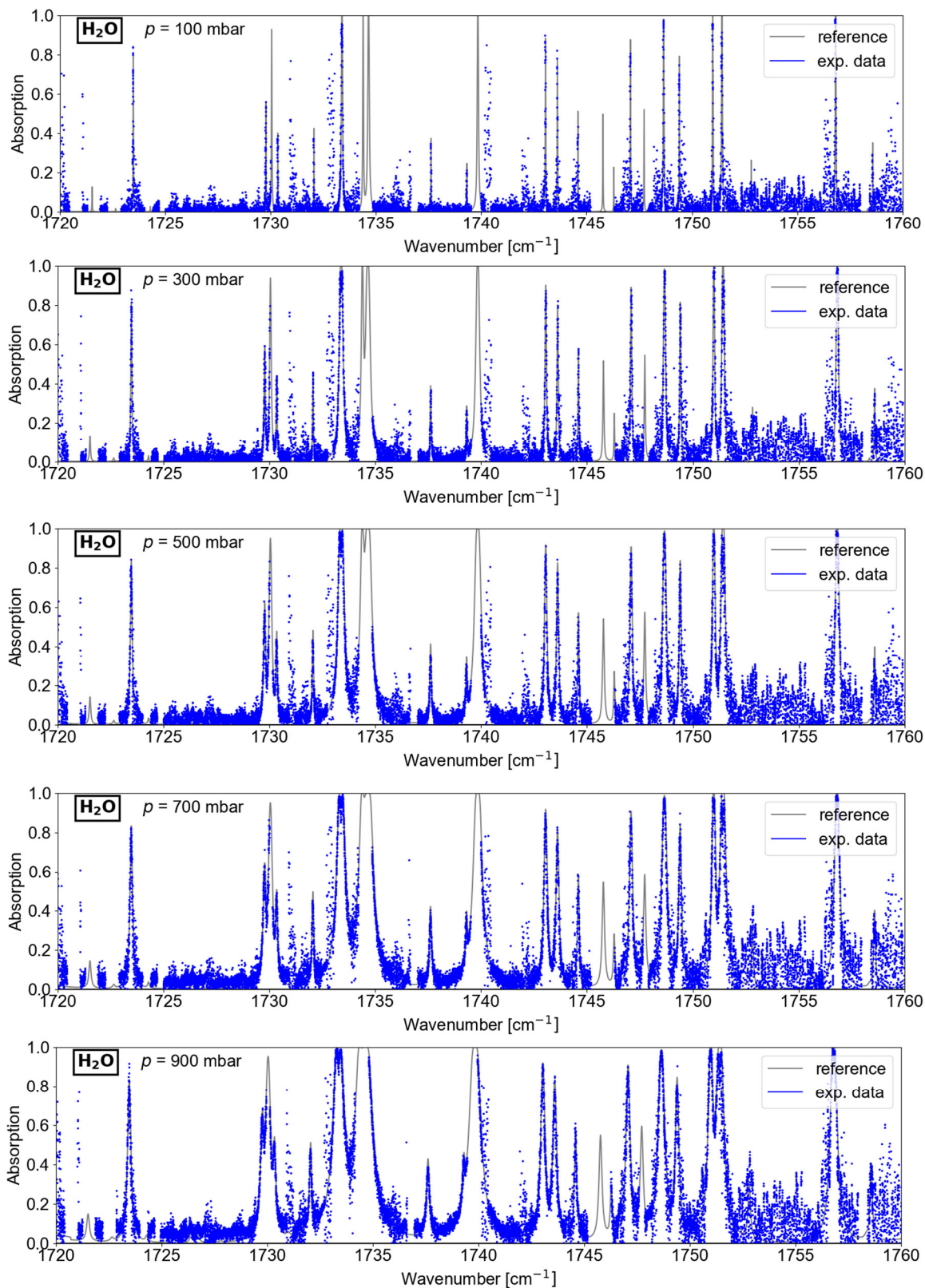
Fig. 45: H₂O measurements at different pressures in external set-up.

The RMS deviation from the reference absorption amplitude is calculated for both species for the full spectra. The results are presented in **Fig. 46**. The N_2O measurement at $p = 900$ mbar and $\Delta t_{stab,I} = 0.001$ s was not evaluable, thus it was omitted from the results and the adjacent measurements points are connected with a dotted line in the figure. The RMS data display a slight tendency to rise with reduced stabilization time. But as before, the change is rather minor. The absolute value of the RMS deviation is higher compared to the internal set-up. That observation can be inferred to the higher noise due to stronger fringing in the external application. It is expected that the RMS should be reduced for an improved beam path where the fringes are further prevented.
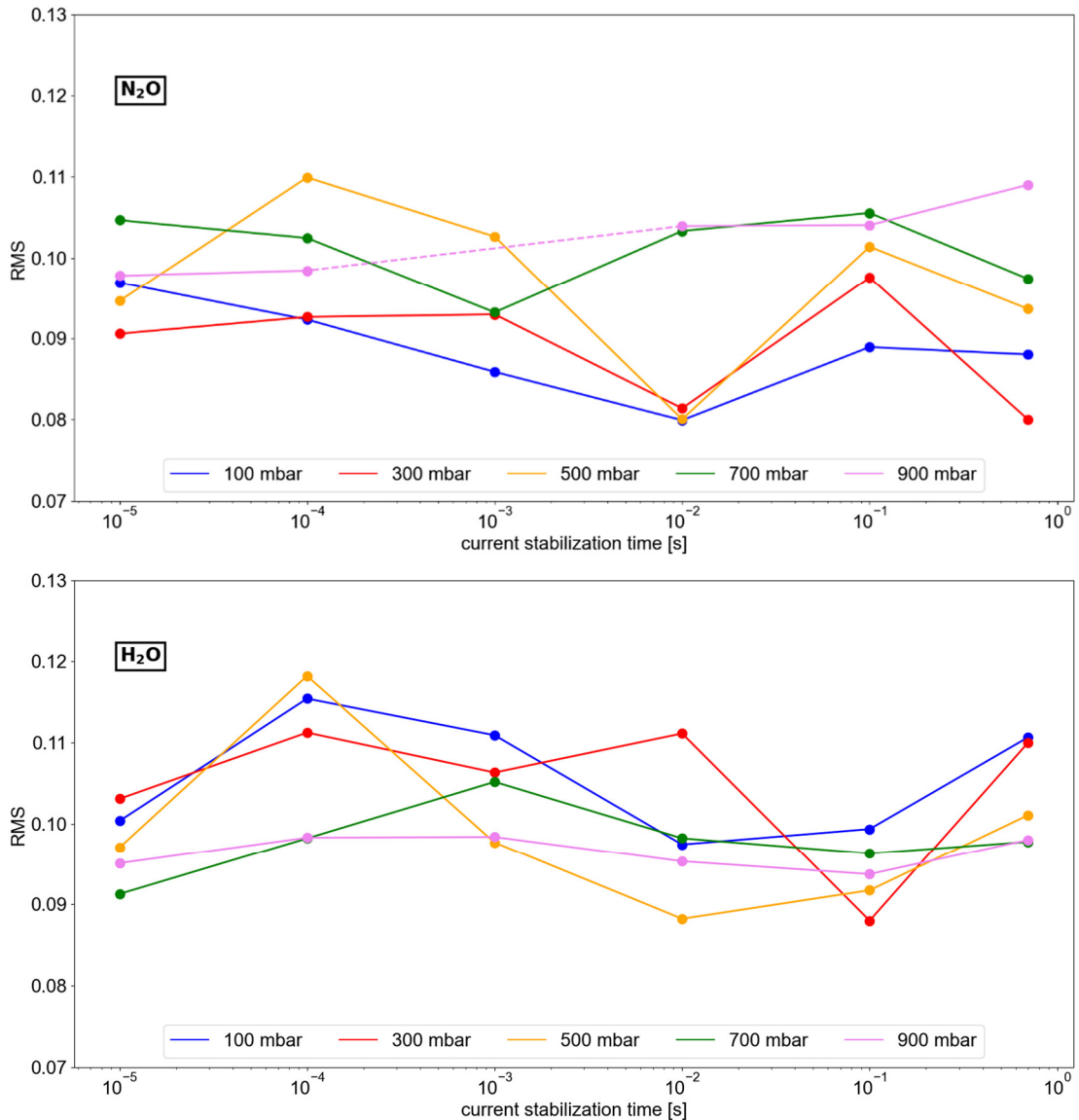
Fig. 46: Calculated RMS of absorption amplitude for N_2O and H_2O measurement at different stabilization times.

5. Summary and Conclusions

The main goals of this work were the establishment of prerequisites for the efficient performance of dual-comb LAS measurements and an investigation of the influence of additional fiber optics. The latter aspect is especially of high relevance for the application of the measurement technique in the HEG where it is necessary to guide the laser beam through the test section with the help of fiber optics.

The outcome of the work are above all technical requirements for conducting calibration measurements. Beside the choice of an appropriate calibration gas species, it was found that it is necessary to purge and evacuate the Herriott test cell appropriately. With regard to the measurement quality, it is helpful to look at the fallback rate that indicates problems with the laser condition itself or issues due to the set-up. It is necessary to analyze whether a baseline offset shift occurs or whether unwanted optical feedback influences the heterodyne signal stability. 100% transmission measurements allow on the one hand to detect wavenumber regions with parasitic gas species. One the other hand, the 100% transmission data of individual comb lines reveal whether there occurs fringing noise and thus further adjustment of the beam path is necessary. The gained knowledge about all these factors will help for carrying out both further calibration measurements and future HEG experiments.

Additionally, comparative measurements in the *LongTerm* and *StepSweeping* measurement modes were conducted for N_2O and ambient H_2O. The increased number of spectral measurement points and thus closing of the large spacing between adjacent points yields better resolved absorption spectra. A finer spectral point spacing enables the complete resolution of absorption features and thus facilitates the identification of species and parameters to derive the concentration from that. Furthermore, it was possible to show that the stabilization time after a current change has a rather small influence on the resulting quality of the measurement in *StepSweeping* mode. This result is promising for upcoming measurements in the *FastSweeping* mode as the *FastSweeping* is sort of an extreme case of stepwise tuning with effectively no stabilization time. In order to prove this hypothesis, it is suggested to carry out measurement in *FastSweeping* and *TimeResolved* measurement mode as next step to continue the calibration.

When changing to an external set-up, new challenges due to the usage of optical fibers arise. An optimal alignment of additional optical elements is required. It was challenging to hit the Brewster angle. The occurring back reflections from the fiber facets caused negative optical feedback. Here, the possibility of an anti-reflection (AR) coating of the SMA connector should be checked as it may prevent optical feedback. The other fiber ends have already an AR coating. The general power loss due to the fibers cannot be overcome and has to be considered in any kind set-up which involves the in- and outcoupling of the beam. The alignment to the Herriott cell is specifically challenging as one needs to hit each mirror perfectly and then guide the beam optimally on the coupler to feed it on the next fiber. The elongated beam path forwards the fringing effect. The alignment on real experimental flight models is supposed to be easier. As the path through the test section will not be longer than 20 cm and does not involve further optical elements like mirrors which is the case for the Herriott cell, it is expected that fringing will play a minor role and is less likely to appear. Nevertheless, it is now a known factor and pre-tests should be conducted in order to confirm a good alignment. Like in the campaign testing the dual-comb LAS [3], there are optical ports manufactured to the model. A port contains an infrared-transparent Zinc-Selenide window. The couplers are mounted on specifically pre-designed holders to align the beam across the line of sight through the model. There are only few angles of freedom with shorter range of motion, so there is less opportunity for fringing.

Despite the mentioned challenges, it was shown that the RMS increases only from around 8% to 11% when switching from the internal to external set-up. This negates the concern that the fibers could lead to a significant worsening of the signal. For further measurements with the described externally placed Herriott cell it is recommended to think about a shield around the set-up that can be evacuated. By that, the beam does not traverse ambient air, which reduces the parasitical water influence and leads to a cleaner spectrum.

In summary, all intended tasks were realized involving the identification of technical necessities, introduction of new measurement modes and aligning of the external set-up. The identification of errors and error sources and thereby derived solutions lay a solid foundation for routines to apply the spectroscopic technique in further calibration measurements and in particular for combustion experiments at HEG. Despite that, it can be concluded that the

measurement technique is of high potential and very promising for high-resolution multi-species measurements during combustion experiments at the HEG if the calibration work is finalized.

Besides the already mentioned future work aspects, a consistent continuation of the calibration work are measurements conducted in the small shock tube should be performed before moving to the HEG. This manually driven shock tube with a total length of around five meters can be used for comparing measurements in *TimeResolved* and *FastSweeping* mode. It is important to perform actual time-resolved measurement with an evolution of gas species concentration to calibrate and evaluate the quality of the time-resolved measurement modes and in particular *FastSweeping* mode.

List of Tables

List of Figures

Literature

[1] B. Khandelwal, A. Karakurt, P. R. Sekaran, V. Sethi, R. Singh: Hydrogen powered aircraft - The future of air transport. *Progress in Aerospace Sciences*. Vol. 60, pp. 45–59. (2013) doi: 10.1016/j.paerosci.2012.12.002.

[2] T. Fortier, E. Baumann: 20 years of developments in optical frequency comb technology and applications. *Commun Phys*. Vol. 2(1), pp. 1–16. (2019) doi: 10.1038/s42005-019-0249-y.

[3] J. Martinez Schramm, D. Luís: Experimental Approach on Concentration Measurements of NO in Hydrogen Combustion Based on Heterodyne Laser Absorption Spectroscopy Using Quantum Cascade Lasers. In: A. Dillmann, G. Heller, E. Krämer, C. Wagner (eds.) : *New Results in Numerical and Experimental Fluid Mechanics XIII*. Vol. 151, pp. 110–120, Springer International Publishing. (2021) doi: 10.1007/978-3-030-79561-0_11.

[4] H. Günzler, H.-U. Gremlich: *IR spectroscopy: an introduction*. Weinheim: Wiley-VCH, (2002).

[5] T. Udem, R. Holzwarth, T. W. Hänsch: Optical frequency metrology. *Nature*. Vol. 416(6877), pp. 233–237. (2002) doi: 10.1038/416233a.

[6] The Nobel Prize in Physics 2005. *NobelPrize.org*. https://www.nobelprize.org/prizes/physics/2005/summary/ (accessed Apr. 12, 2022).

[7] G. F. F. Villares: Quantum cascade laser frequency combs for spectroscopy applications. PhD thesis. ETH Zurich. (2016). doi: 10.3929/ethz-a-010780121.

[8] G. Villares, A. Hugi, S. Blaser, J. Faist: Dual-comb spectroscopy based on quantum-cascade-laser frequency combs. *Nat Commun*. Vol. 5(1), p. 5192. (2014) doi: 10.1038/ncomms6192.

[9] J. Faist, G. Villares, G. Scalari, M. Rösch, C. Bonzon, A. Hugi, M. Beck: Quantum Cascade Laser Frequency Combs. *Nanophotonics*. Vol. 5(2), pp. 272–291. (2016) doi: 10.1515/nanoph-2016-0015.

[10] N. Opacak: The origin of frequency combs in free-running quantum cascade lasers. PhD thesis. Technische Universität Wien. (2022).

[11] R. F. Kazarinov, R. A. Suris: Possibility of the Amplification of Electromagnetic Waves in a Semiconductor with a Superlattice. *Soviet Physics - Semiconductors*. Vol. 5(4), pp. 797–800. (1971).

[12] J. Faist, F. Capasso, D. L. Sivco, C. Sirtori, A. L. Hutchinson, A. Y. Cho: Quantum Cascade Laser. *Science*. Vol. 264(5158), pp. 553–556. (1994) doi: 10.1126/science.264.5158.553.

[13]   A. Hugi: Single-mode and comb operation of broadband quantum cascade lasers. PhD thesis. ETH Zurich. (2013). doi: 10.3929/ethz-a-009908406.

[14]   H. A. Haus: Mode-locking of lasers. *IEEE Journal of Selected Topics in Quantum Electronics*. Vol. 6(6), pp. 1173–1185. (2000) doi: 10.1109/2944.902165.

[15]   B. Schwarz, D. Ristanic, P. Reininger, T. Zederbauer, D. MacFarland, H. Detz, A. M. Andrews, W. Schrenk, G. Strasser: High performance bi-functional quantum cascade laser and detector. *Appl. Phys. Lett.* Vol. 107(7), p. 071104. (2015) doi: 10.1063/1.4927851.

[16]   A. Hugi, G. Villares, S. Blaser, H. C. Liu, J. Faist: Mid-infrared frequency comb based on a quantum cascade laser. *Nature*. Vol. 492(7428), pp. 229–233. (2012) doi: 10.1038/nature11620.

[17]   C. J. Jachimowski: An Analytica1Study of the Hydrogen-Air Reaction Mechanism With Application to Scramjet Combustion. NASA Technical Paper 2791. (1988).

[18]   M. Dharavath, P. Manna, D. Chakraborty: Thermochemical exploration of hydrogen combustion in generic scramjet combustor. *Aerospace Science and Technology*. Vol. 24(1), pp. 264–274. (2013) doi: 10.1016/j.ast.2011.11.014.

[19]   Y. Zeldovich, D. Frank-Kamenetskii, P. Sadovnikov: Oxidation of Nitrogen in Combustion and Explosions. In: R. Alievich Sunyaev (ed.) : *Selected Works of Yakov Borisovich Zeldovich, Volume I: Chemical Physics and Hydrodynanics*, pp. 404–410, Princeton University Press. (1992) doi: 10.1515/9781400862979.404.

[20]   V. Knop, A. Benkenida, S. Jay, O. Colin: Modelling of combustion and nitrogen oxide formation in hydrogen-fuelled internal combustion engines within a 3D CFD code. *International Journal of Hydrogen Energy*. Vol. 33(19), pp. 5083–5097. (2008) doi: 10.1016/j.ijhydene.2008.06.027.

[21]   G. A. Lavoie, J. B. Heywood, J. C. Keck: Experimental and Theoretical Study of Nitric Oxide Formation in Internal Combustion Engines. *Combustion Science and Technology*. Vol. 1(4), pp. 313–326. (1970) doi: 10.1080/00102206908952211.

[22]   M. Ciniviz, H. Köse: Hydrogen Use in Internal Combustion Engine: A Review.(2012).

[23]   J. Pletzer, D. Hauglustaine, Y. Cohen, P. Jöckel, V. Grewe: The climate impact of hydrogen-powered hypersonic transport. *Atmospheric Chemistry and Physics*. Vol. 22(21), pp. 14323–14354. (2022) doi: 10.5194/acp-22-14323-2022.

[24]   F. Svensson, A. Hasselrot, J. Moldanova: Reduced environmental impact by lowered cruise altitude for liquid hydrogen-fuelled aircraft. *Aerospace Science and Technology*. Vol. 8(4), pp. 307–320. (2004) doi: 10.1016/j.ast.2004.02.004.

[25]   F. Haglind, A. Hasselrot, R. Singh: Potential of reducing the environmental impact of aviation by using hydrogen Part II: Aero gas turbine design. *The Aeronautical Journal*. Vol. 110(1110), pp. 541–552. (2006) doi: 10.1017/S0001924000028967.

[26]   T. K. Tromp, R.-L. Shia, M. Allen, J. M. Eiler, Y. L. Yung: Potential Environmental Impact of a Hydrogen Economy on the Stratosphere. *Science*. Vol. 300(5626), pp. 1740–1742. (2003) doi: 10.1126/science.1085169.

[27]   D. Cecere, E. Giacomazzi, A. Ingenito: A review on hydrogen industrial aerospace applications. *International Journal of Hydrogen Energy*. Vol. 39(20), pp. 10731–10747. (2014) doi: 10.1016/j.ijhydene.2014.04.126.

[28]   F. Haglind, A. Hasselrot, R. Singh: Potential of reducing the environmental impact of aviation by using hydrogen Part I: Background, prospects and challenges. *The Aeronautical Journal*. Vol. 110(1110), pp. 533–540. (2006) doi: 10.1017/S000192400000141X.

[29]   H. Johnston: Reduction of Stratospheric Ozone by Nitrogen Oxide Catalysts from Supersonic Transport Exhaust. *Science*. Vol. 173(3996), pp. 517–522. (1971) doi: 10.1126/science.173.3996.517.

[30]   A. Ingenito, A. Agresta, R. Andriani, F. Gamma: NOx reduction strategies for high speed hydrogen fuelled vehicles. *International Journal of Hydrogen Energy*. Vol. 40(15), pp. 5186–5196. (2015) doi: 10.1016/j.ijhydene.2015.02.100.

[31]   R. V. Kochanov, I. E. Gordon, L. S. Rothman, P. Wcisło, C. Hill, J. S. Wilzewski: HITRAN Application Programming Interface (HAPI): A comprehensive approach to working with spectroscopic data. *Journal of Quantitative Spectroscopy and Radiative Transfer*. Vol. 177, pp. 15–30. (2016) doi: 10.1016/j.jqsrt.2016.03.005.

[32]   I. E. Gordon *et al.*: The HITRAN2020 molecular spectroscopic database. *Journal of Quantitative Spectroscopy and Radiative Transfer*. Vol. 277, p. 107949. (2022) doi: 10.1016/j.jqsrt.2021.107949.

[33]   A. Mohamed, B. Rosier, D. Henry, Y. Louvet, P. L. Varghese: Tunable diode laser measurements on nitric oxide in a hypersonic wind tunnel. *AIAA Journal*. Vol. 34(3), pp. 494–499. (1996) doi: 10.2514/3.13095.

[34]   C. T. Bowman: Investigation of Nitric Oxide Formation Kinetics in Combustion Processes: The Hydrogen-Oxygen-Nitrogen Reaction. *Combustion Science and Technology*. Vol. 3(1), pp. 37–45. (1971) doi: 10.1080/00102207108952269.

[35]   C. A. Almodovar, R. M. Spearrin, R. K. Hanson: Two-color laser absorption near 5μm for temperature and nitric oxide sensing in high-temperature gases. *Journal of Quantitative Spectroscopy and Radiative Transfer*. Vol. 203, pp. 572–581. (2017) doi: 10.1016/j.jqsrt.2017.03.003.

[36]   J. J. Girard, P. M. Finch, C. L. Strand, R. K. Hanson, W. M. Yu, J. M. Austin, H. G. Hornung: Measurements of Reflected Shock Tunnel Freestream Nitric Oxide

Temperatures and Partial Pressure. *AIAA Journal*. Vol. 59(12), pp. 5266–5275. (2021) doi: 10.2514/1.J060596.

[37]   B. J. Wheatley: Applications of Tunable Diode Laser Absorption Spectroscopy to Aerospace Flows. University of Queensland. (2017).

[38]   D. Herriott, H. Kogelnik, R. Kompfner: Off-Axis Paths in Spherical Mirror Interferometers. *Appl. Opt.* Vol. 3(4), p. 523. (1964) doi: 10.1364/AO.3.000523.

[39]   R.-A. Lorbeer, O. Kliebisch, P. Mahnke, C. B. Ortega, F. D. Capua, J. Weber, M. Damm: Pressure detection via tunable diode laser spectroscopy in the oxygen A-Band. In: *Optical Sensors and Sensing Congress*. p. SM1B.6. (2020) doi: 10.1364/SENSORS.2020.SM1B.6.

[40]   J. Weber: Berührungslose Luftfeuchtigkeitsbestimmung mittels Laserspektroskopie. Master's Thesis. Hochschule Furtwangen. (2020). Accessed: Nov. 16, 2022. [Online]. Available: https://elib.dlr.de/137248/

[41]   R. Ghorbani, F. M. Schmidt: Real-time breath gas analysis of CO and CO2 using an EC-QCL. *Appl. Phys. B*. Vol. 123(5), p. 144. (2017) doi: 10.1007/s00340-017-6715-x.

[42]   IRcell-S – IRsweep. https://irsweep.com/products/ircell/ (accessed Nov. 16, 2022).

[43]   B. Tuzson, M. Mangold, H. Looser, A. Manninen, L. Emmenegger: Compact multipass optical cell for laser spectroscopy. *Opt. Lett., OL*. Vol. 38(3), pp. 257–259. (2013) doi: 10.1364/OL.38.000257.

Appendix

I.   Measurement Settings

LongTerm measurements

Parameter	Value
Current 1	835.9 mA
Current 2	899.2 mA
Temperature 1	-8.85°C
Temperature 2	-13.25°C

StepSweeping measurements

Parameter	Value
Current 1	835.9 mA – 845.58 mA (in 54 steps)
Current 2	899.2 mA – 908.08 mA (in 54 steps)
Temperature 1	[-8.85°C, -8.02°C, -7.215°C]
Temperature 2	[-13.25°C, -12.45°C, -11.65°C]

Erklärung

Ich versichere hiermit, dass ich die vorliegende Arbeit ohne fremde Hilfe selbstständig verfasst und nur die von mir angegebenen Quellen und Hilfsmittel verwendet habe. Wörtlich oder sinngemäß aus anderen Werken entnommene Stellen habe ich unter Angabe der Quellen kenntlich gemacht. Die Richtlinien zur Sicherung der guten wissenschaftlichen Praxis an der Universität Göttingen wurden von mir beachtet. Eine gegebenenfalls eingereichte digitale Version stimmt mit der schriftlichen Fassung überein. Mir ist bewusst, dass bei Verstoß gegen diese Grundsätze die Prüfung mit nicht bestanden bewertet wird.

Göttingen, den 17. Januar 2023   Leni Schmidt